Evidence for strong electron-phonon coupling in $MgCNi_3$

A. Wälte, G. Fuchs,* K.-H. Müller, A. Handstein, K. Nenkov,† V. N. Narozhnyi,‡ S.-L. Drechsler, S. Shulga,§ and L. Schultz
Institut für Festkörper- und Werkstoffforschung Dresden, Postfach 270116, D-01171 Dresden, Germany

H. Rosner
Max-Planck-Institut für Chemische Physik fester Stoffe, Nöthnitzer Strasse 40, D-01187 Dresden, Germany
(Received 30 January 2003; revised manuscript received 26 May 2004; published 5 November 2004)

The title compound is investigated by specific heat measurements in the normal and superconducting states supplemented by upper critical field transport, susceptibility, and magnetization measurements. From a detailed analysis including also full potential electronic structure calculations for the Fermi surface sheets, Fermi velocities, and partial densities of states the presence of both strong electron-phonon interactions and considerable pair breaking has been revealed. The specific heat and the upper critical field data can be described to a first approximation by an effective single-band model close to the clean limit derived from a strongly coupled predominant hole subsystem with small Fermi velocities. However, in order to account also for Hall-conductivity and thermopower data in the literature, an effective general two-band model is proposed. This two-band model provides a flexible enough frame to describe consistently all available data within a scenario of phonon mediated *s*-wave superconductivity somewhat suppressed by a sizable electron-paramagnon or electron-electron Coulomb interaction. For quantitative details the relevance of soft phonons and of a Van Hove–type singularity in the electronic density of states near the Fermi energy is suggested.

DOI: 10.1103/PhysRevB.70.174503 PACS number(s): 74.70.Ad

I. INTRODUCTION

The recent discovery of superconductivity in the intermetallic antiperovskite compound $MgCNi_3$ (Ref. 1) with a superconducting transition temperature of $T_c \simeq 8$ K is rather surprising considering its high Ni content. Therefore it is expected that this compound is near a ferromagnetic instability which might be reached by hole doping on the Mg sites.[2] The possibility of unconventional superconductivity due to the proximity of these two types of collective order has attracted great interest in the electronic structure and the physics of the pairing mechanism.

Band structure calculations[2–6] for $MgCNi_3$ revealed a domination of the electronic states at the Fermi surface by the 3*d* orbitals of Ni, suggesting the presence of ferromagnetic spin fluctuations.[2,4] ^{13}C NMR measurements[7] result in Fermi liquid behavior with an electronic crossover at $T \approx 50$ K and a growing formation of spin fluctuations below $T \approx 20$ K. Resistivity measurements,[1,8,9] measurements of the thermopower, the thermal conductivity and the magnetoresistance,[10] doping experiments,[9,11] and magnetization measurements[11] are consistent with this interpretation.

$MgCNi_3$ has been considered as a structurally related compound of the layered transition metal borocarbides which exhibit superconducting transition temperatures up to ≈ 23 K.[11,12] In spite of the much lower T_c of $MgCNi_3$, its upper critical field H_{c2} at low temperatures, $H_{c2}(0) = 8-15$ T,[8,13–16] is comparable with that of the borocarbides or even higher. However, a rather different and unusual shape, especially near T_c, for the temperature dependence of $H_{c2}(T)$ is observed for the latter compounds.[17] At variance the $H_{c2}(T)$ dependence of $MgCNi_3$ is similar to that of usual superconductors which are described reasonably well within the isotropic single-band approximation and exhibit a steep linear slope of $H_{c2}(T)$ at T_c.

Through analysis of specific heat data, $MgCNi_3$ was characterized in the framework of a conventional, phonon-mediated pairing both as a moderate[1,16] and as a strong[14,18] coupling superconductor. Strong coupling is also suggested by measurements of the thermopower[10] and the large energy gap determined from tunneling experiments.[14] The question of the pairing symmetry is controversially discussed in the literature. ^{13}C NMR experiments,[7] specific heat measurements,[16] and tunneling spectra[19] support *s*-wave pairing in $MgCNi_3$, whereas earlier tunneling spectra[14] and penetration depth measurements[20] have been interpreted in terms of an unconventional pairing state. Recent measurements of the critical current of $MgCNi_3$ may be interpreted in the latter sense, too.[21]

In the present investigation, specific heat data of $MgCNi_3$ in the normal and superconducting states were analyzed in detail with the aid of a realistic phonon model and strong coupling corrections as suggested by Carbotte.[22] The results are brought into accordance with the two-band character of $MgCNi_3$ emerging from band structure calculations and a parallel analysis of the upper critical field $H_{c2}(0)$, in order to find out a consistent physical picture explaining at least qualitatively various available experimental results.

II. ESSENTIALS OF THE THEORETICAL ELECTRONIC STRUCTURE

Following previous work[2] in the present section we remind the reader of some essential features and point out details of the electronic structure of $MgCNi_3$ which are crucial for a proper interpretation of the specific heat [total and

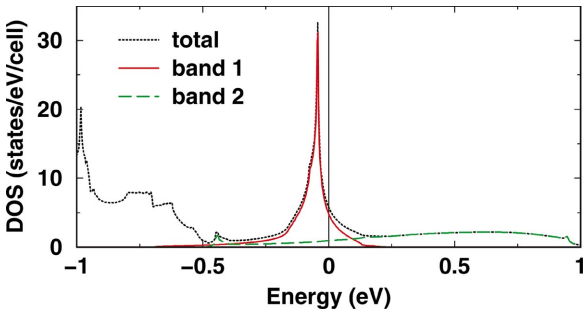

FIG. 1. (Color) Partial density of states of the two bands in $MgCNi_3$ corresponding to the two Fermi surface sheets shown in Fig. 2. Dotted line: total density of states.

Fermi surface sheet (FSS) related partial densities of states (DOS)], upper critical field, and transport data (topology of the Fermi surface and the magnitude of the Fermi velocities). Among various band structure calculations there is general consensus about the qualitative topology of the Fermi surface and the presence of a strong peak (Van Hove singularity) in $N(E)$ slightly below the Fermi energy. At the same time there are clear differences with respect to the magnitudes of $N(0)=4.8$ states/eV$=11$ mJ/mol K^2 [to be compared with 4.63 states/eV (Ref. 3), 4.99 states/eV (Ref. 4), 5.34 states/eV (Ref. 6)] and especially with respect to the Stoner factor $S=3.3$ [compared with 1.75 (Ref. 3), 2.78 (Ref. 23), to 5 (Ref. 4)] as well as to the distance of the DOS peak 42 meV [compared with 40 meV (Ref. 24) to 80 meV (Ref. 23)] below E_F. The peak may be of relevance for a proper quantitative description of the electronic specific heat, transport data, magnetic properties, and superconductivity. Last but not least, there is also a sizable variety on the magnitude of the electron-phonon coupling constant λ_{ph} (ranging between 0.8 and 2.0) mainly caused by poor knowledge of the phonon energies and possible lattice anharmonicities.[24]

Our results have been obtained by a band structure calculation code using the full-potential nonorthogonal local-orbital (FPLO) minimum-basis scheme.[25] There are about 0.285 charges per unit cell with exactly equal numbers of holes and electrons—i.e., $n_h=n_{el}$—which follows from the even number of electrons per unit cell [to distinguish both bands, we will use the index "h" for the hole band ("1") and "el" for the electron band ("2") in the following analysis]. In other words, $MgCNi_3$ is a so-called compensated metal which must be described in terms of multiband model by definition. Thus, it makes sense to start with a two-band model. The generalization to any higher multiband scenario is straightforward. A standard single-band system with an even number of electrons per unit cell would be a band insulator. Thus, metallicity is achieved owing to the two-band character which leads to electron and hole-derived FSS's. The total DOS $N(0)$ at the Fermi level can be decomposed into a roughly 85% and a 15% contribution stemming from two-hole and two-electron sheets of the Fermi surface, respectively (see Figs. 1 and 2). The two types of hole sheets are formed by eight droplets (ovoids) oriented along the spatial diagonals of the cube—i.e., along the Γ-R lines and six FSS with a "four-leaved-clover"-like shape centered at the X points in the middle of the faces of the cube (see Fig. 2). The

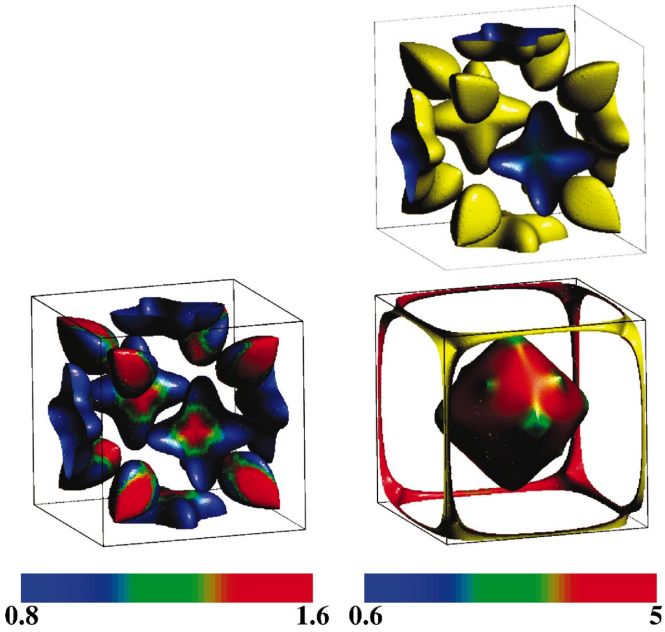

FIG. 2. (Color) Fermi surface sheets of $MgCNi_3$. Fermi velocities are measured in different colors (see scales below the figure) in units of 10^7 cm/s; i.e., blue color stands for slow and red color for fast quasiparticles. Upper panel and lower left panel: hole sheets corresponding to "band 1" in Fig. 1. Lower right panel: electron sheets corresponding to "band 2" in Fig. 1. The right panels present the Fermi velocity distribution of the two sheets on the same absolute scale to demonstrate the slow (heavy) character of the holes. Yellow color: sides of filled electrons. The left panel shows the v_F-distribution in the hole sheets on a smaller scale in more detail.

coordinates of the symmetry points read $\Gamma=(0,0,0)$, $R=(0.5,0.5,0.5)$, $X=(0.5,0,0)$, and $M=(0.5,0.5,0)$ (all given in units of $2\pi/a$, where $a=0.381$ nm is the lattice constant). The FSS's with electron character are given by the rounded cube centered at Γ and 12 thin jungle gims spanning from R to M.

The band structure calculations provide us directly with several material parameters (total and partial densities of states, Fermi velocities, etc.) important for the understanding of superconductivity and electronic transport properties. For instance the transport properties are described by quadratically averaged Fermi velocities $\langle v^2\rangle_{FSS}$ whereas the upper critical field is described by averages of the type $\langle 1/v^2\rangle_{FSS}$ which yields a smaller effective velocity in general. Using the general definitions of the local density of states (in $\vec{k}$ space) and those of mth and the first moments of the Fermi velocity $v=|\vec{v}(\vec{k})|$, respectively, we have

$$\langle v^m\rangle_i = \frac{\int dS_i N_i(\vec{k})|\vec{v}_i(\vec{k})|^m}{\int dS_i N_i(\vec{k})} \equiv \frac{\int dS_i|\vec{v}_i(\vec{k})|^{m-1}}{\int 4\pi^3\hbar N_i(0)},$$

$$\langle v\rangle_i \equiv \overline{v_i} = \frac{S_{F,i}}{4\pi^3\hbar N_i(0)},$$

$$\langle v^{\mathrm{m}}\rangle_i = \frac{\overline{v_i}\int \mathrm{d}S_i|\vec{v}(\vec{k})|^{m-1}}{S_{\mathrm{F},i}},$$

where $i=\mathrm{el},\mathrm{h},\mathrm{tot}$, $S_{\mathrm{F},i}$ denotes the area of the ith Fermi surface sheet, and the effective quantity is related to the linearly averaged value $\overline{v}$ adopting a simple estimate as

$$\langle v^{-2}\rangle_i = \frac{\overline{v_i}\int \mathrm{d}S_i|\vec{v}_i(\vec{k})|^{-3}}{S_{\mathrm{F},i}} \equiv v_{\mathrm{hc2},i}^{-2},$$

$$v_{\mathrm{hc2}} \approx \overline{v}[1-(\delta v/\overline{v})^2],$$

where δv is the halfwidth of the v distribution. For the two above-mentioned subgroups of quasiparticles we estimate $\overline{v_{\mathrm{el}}}=3.9\times10^7$ cm/s and $\overline{v_{\mathrm{h}}}=1.2\times10^7$ cm/s, $v_{\mathrm{tr,h}}=1.11\times10^7$ cm/s, $v_{\mathrm{hc2,h}}=1.07\times10^7$ cm/s, and $v_{\mathrm{tr,el}}=4.89\times10^7$ cm/s, where $\delta v_{\mathrm{h}}=4\times10^6$ cm/s and $\delta v_{\mathrm{el}}=1.1\times10^7$ cm/s have been used (compare also Fig. 2).

Finally, in the isotropic single-band (ISB) model realized in the extreme dirty limit of superconductivity one arrives at

$$N(0)v_{\mathrm{tr,ISB}}^2 = N_{\mathrm{h}}(0)v_{\mathrm{tr,h}}^2 + N_{\mathrm{el}}(0)v_{\mathrm{tr,el}}^2,$$

which yields $v_{\mathrm{tr,ISB}}=2.15\times10^7$ cm/s in accordance with Ref. 3. The corresponding plasma energy amounts to $\hbar\omega_{\mathrm{pl}}=3.17$ eV close to 3.25 eV given in Ref. 4. Naturally, the total plasma frequency ω_{pl} can be also decomposed into the plasma frequencies of both subsystems:

$$\omega_{\mathrm{pl}}^2 = \omega_{\mathrm{pl,h}}^2 + \omega_{\mathrm{pl,el}}^2 = \omega_{\mathrm{pl,h}}^2\left(1+\frac{N_2(0)v_{\mathrm{tr},2}^2}{N_1(0)v_{\mathrm{tr},1}^2}\right).$$

Thus we estimate $\hbar\omega_{\mathrm{pl,h}}\approx1.89-1.94$ eV and $\hbar\omega_{\mathrm{pl,el}}\approx2.55-2.61$ eV. From these partial plasma energies a useful relation between the scattering rates $\gamma_{\mathrm{imp},i}$ and the conductivities σ_i (with $i=\mathrm{h},\mathrm{el}$) in both subsystems can be obtained:

$$\frac{\gamma_{\mathrm{imp,el}}}{\gamma_{\mathrm{imp,h}}} = 1.816\frac{\sigma_{\mathrm{h}}}{\sigma_{\mathrm{el}}} = 1.816\frac{\rho_{\mathrm{el}}}{\rho_{\mathrm{h}}},$$

where ρ_i denotes the corresponding resistivity. In the present case the disorder is expected to be caused mainly by Mg- and C-related defects such as vacancies and interstitials. Therefore the ratio of the scattering rates might scale with the ratio of the non-Ni-derived Mg and C orbital partial densities of states at the Fermi level and the corresponding Fermi velocities. As a result we estimate from our local density approximation (LDA) FPLO calculations

$$\left(\frac{\gamma_{\mathrm{imp,el}}}{\gamma_{\mathrm{imp,h}}}\right)_{\mathrm{LDA}} \approx \frac{N_{\mathrm{el,Mg,C}}(0)v_{\mathrm{el}}}{N_{\mathrm{h,Mg,C}}(0)v_{\mathrm{h}}} \approx 4.81. \qquad (1)$$

Within this approach the corresponding mean free paths differ by a factor of 0.917 and a conductivity ratio of $\sigma_{\mathrm{h}}/\sigma_{\mathrm{el}}=1.403$ would be expected.

In the following analysis we usually make use of $\hbar=k_{\mathrm{B}}=\mu_0=1$ for the sake of simplification.

III. EXPERIMENT

Polycrystalline samples of $MgCNi_3$ have been prepared by solid-state reaction. In order to obtain samples with high T_c, we used an excess of carbon as proposed in Ref. 1. To cover the high volatility of Mg during sintering of the samples an excess of Mg is used.[1] In this study, a sample with the nominal formula $Mg_{1.2}C_{1.6}Ni_3$ has been investigated and is denoted as $MgC_{1.6}Ni_3$. To prepare the sample a mixture of Mg, C, and Ni powders was pressed into a pellet. The pellet was wrapped in a Ta foil and sealed in a quartz ampoule containing an Ar atmosphere at 180 mbar. The sample was sintered for half an hour at 600 °C followed by one hour at 900 °C. After a cooling process the sample was reground. This procedure was repeated 2 times in order to lower a possible impurity phase content. The obtained sample was investigated by x-ray diffractometry to estimate its quality. The diffractometer pattern (Fig. 3) shows small impurity concentrations mainly resulting from MgO and unreacted carbon crystallized as graphite (≈10 vol. %). The lattice constant of the prepared sample was determined to be $a=0.38107(1)$ nm using the Rietveld code FULLPROF.[26] This indicates that the nearly single-phase sample corresponds to the superconducting modification of MgC_xNi_3.[27] The superconducting transition of the sample was investigated by measurements of electrical resistance, ac susceptibility, and specific heat. For the electrical resistance measurement a piece cut from the initially prepared pellet with 5 mm in length and a cross section of approximately 1 mm^2 was measured in magnetic fields up to 16 T using the standard four-probe method with current densities between 0.2 and 1 A/cm^2. The ac susceptibility and the specific heat measurements were performed on other pieces from the same pellet in magnetic fields up to 9 T.

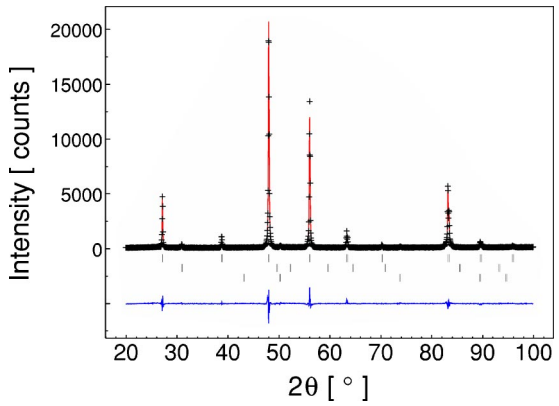

FIG. 3. (Color online) Rietveld refinement for the $MgC_{1.6}Ni_3$ sample. The crosses correspond to the experimental data. The solid line shows the calculated pattern. The vertical bars give the Bragg positions for the main phase $MgCNi_3$, for graphite and MgO (from top to bottom). The black line at the bottom of the plot gives the difference between the experimental and calculated pattern.

IV. RESULTS

A. Resistivity

The temperature dependence of the electrical resistance of the investigated sample is shown in Fig. 4. A superconducting transition with an onset (midpoint) value of $T_c=7.0$ K (6.9 K) is observed (see inset of Fig. 4) which coin-

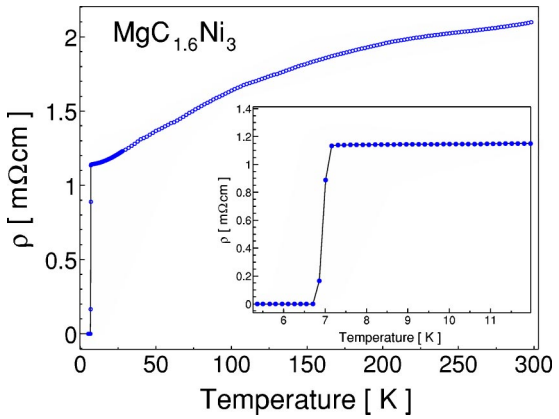

FIG. 4. (Color online) Resistivity as a function of temperature of the $MgC_{1.6}Ni_3$ sample up to room temperature. The inset shows the superconducting transition region.

cides with the onset of the superconducting transition of $T_c = 7.0$ K determined from ac susceptibility. Its residual resistance ratio $\rho(300\ \mathrm{K})/\rho(8\ \mathrm{K}) = 1.85$ and the shape of the $\rho(T)$ curve are typical for $MgCNi_3$ powder samples.[1,8,9] It should be noted that the sample of Fig. 4 has a resistivity of $\rho_{300\ \mathrm{K}} = 2.1\ \mathrm{m}\Omega$ cm which is much too large in order to be intrinsic.

The nonintrinsic origin of the corresponding residual resistivity of $\rho_0 = 1.13\ \mathrm{m}\Omega$ cm follows from reasonable values for the mean free path which has to exceed the lattice constant a according to the Joffe-Regel limit $l_{\mathrm{imp}} \geqslant a$.[28,29] Using $v_F = v_{\mathrm{tr,ISB}} = 2.15 \times 10^7$ cm/s and $\omega_{\mathrm{pl}} = 3.17$ eV from Sec. II, the maximal intrinsic residual resistivity is estimated as $\rho_0^{\max} = 4\pi v_F/(\omega_{\mathrm{pl}}^2 a) = 0.29\ \mathrm{m}\Omega$ cm, in the extreme isotropic single-band dirty limit.

A natural explanation for the high resistivity of the investigated sample which was not subjected to high-pressure sintering is a relatively large resistance of the grain boundaries.[9] This conclusion is supported by $H_{c2}(0)$ and T_c values of recent low-resistivity thin film data (with ρ_0 down to 20 $\mu\Omega$ cm) by Young *et al.*,[15] which are comparable to available powder sample values.

B. Specific heat

Specific heat measurements were performed in order to get information about the superconducting transition, the upper critical field, and the superconducting pairing symmetry and the strength of the electron-phonon coupling from thermodynamic data. In Fig. 5 specific heat data c_p/T vs T^2 are shown for applied magnetic fields up to 8 T. The previously mentioned (see Sec. III) 10 vol. % graphite impurity contribution, corresponding to $\approx 0.2\% - 0.3\%$ of total specific heat at 2–30 K, was subtracted according to Ref. 30.

The specific heat can be considered as a sum of a lattice contribution and a linear-in-T term which gives the electronic contribution with γ_N^* as the Sommerfeld parameter:

$$c_n(T) = \gamma_N^* T + c_{\mathrm{lattice}}(T). \tag{2}$$

To extract the lattice contribution of the normal-state specific heat the low-temperature limit

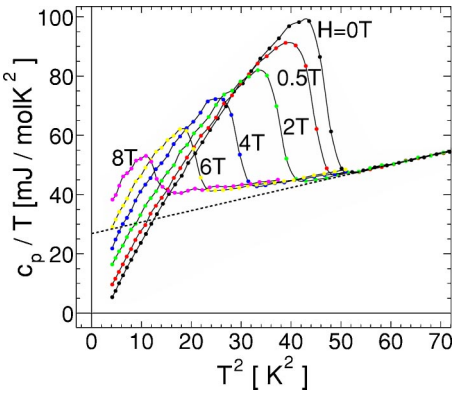

FIG. 5. (Color online) Specific heat data c_p/T vs T^2 of $MgC_{1.6}Ni_3$ measured at various magnetic fields up to 8 T. The dashed line is a fit of the Debye approximation to the data for $H = 0$ T above T_c. Its intersection with the c_p/T axis gives the Sommerfeld parameter $\gamma_N^* = 27$ mJ/mol K^2 (see text).

$$c_{\mathrm{lattice}}(T) = \beta T^3 \tag{3}$$

of the Debye model is usually applied. A fit of Eq. (2) to the data is shown in Fig. 5, resulting in the parameters $\beta = 0.39$ mJ K^2/mol and $\gamma_N^* = 27.0$ mJ/mol K^2. Notice that the Sommerfeld parameter is connected to the electron-phonon coupling strength by $\gamma_N^* = \gamma_0(1 + \lambda_{\mathrm{ph}})$. With $\gamma_0 = 11$ mJ/mol K^2 (Sec. II), one obtains $\lambda_{\mathrm{ph}} = 1.45$, in contradiction with recently reported medium coupling results.[1,16] From the lattice contribution the Debye temperature $\Theta_D^* = 292$ K was derived. Both parameters (Θ_D^*, γ_N^*) are consistent with what has been reported so far.[14,16] The fit describes the normal-state data above T_c but its extrapolation to $T = 0$ K obviously underestimates the high-field data (see Fig. 5).

The transition temperature $T_c = 6.8$ K, calculated from entropy conservation criterion, agrees well with the transition temperatures $T_c = 6.9$ K and $T_c = 7.0$ K derived from resistance and ac susceptibility data, respectively.

The jump $\Delta c(T = T_c)$ of the specific heat is given by the difference between the experimental data, $c_p(T)$ and the normal-state specific heat contribution $c_n(T)$. Notice that the experimental value of the jump, $\Delta c(T_c)/(\gamma_N T_c) = 2.09$ (derived from an entropy conserving construction—see Sec. V B), is strongly enhanced compared to the BCS value (1.43), indicating strong electron-phonon coupling.

C. Superconducting transition and upper critical field

The field dependence of the electrical resistance of our investigated sample is shown in Fig. 6 for several temperatures between 1.9 and 6.0 K. A sharp transition is observed. It remains sharp down to low temperatures. In Fig. 7, the field values H_{10}, H_{50}, and H_{90} defined at 10%, 50%, and 90% of the normal-state resistance are plotted as a function of temperature. Identical results have been found from resistance-vs-temperature transition curves measured at different magnetic fields. Additionally, Fig. 7 shows upper critical field data determined from ac susceptibility measurements, H_{c2}^{sus}, determined by an onset criterion.

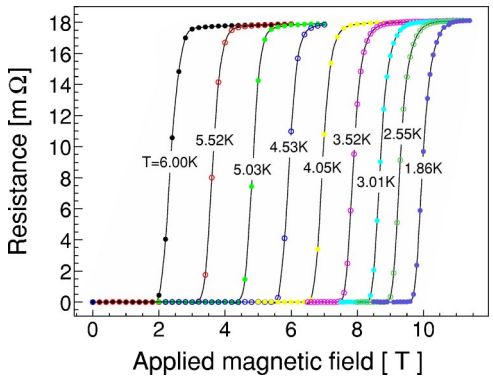

FIG. 6. (Color online) Resistivity of the $MgC_{1.6}Ni_3$ sample as a function of the applied magnetic field for various fixed temperatures as labeled.

It is clearly seen that for the investigated sample H_{c2}^{sus} agrees approximately with H_{10}. A similar behavior was already observed for MgB_2, whereas in the case of rare-earth nickel borocarbides the onset of superconductivity determined from ac susceptibility was typically found to agree well with the midpoint value (H_{50}) of the normal-state resistivity. The width $\Delta H = H_{90} - H_{10}$ of the superconducting transition curves in Fig. 6 (and Fig. 7) remains, with $\Delta H \simeq 0.6$ T, almost unchanged down to low temperatures. A nontextured polycrystalline sample of a strongly anisotropic superconductor shows a gradual broadening of the superconducting transition with decreasing temperature as was observed, for example, for MgB_2.[31] Therefore, the nearly constant transition width ΔH observed for the investigated sample can be considered as an indication of a rather small anisotropy of $H_{c2}(T)$ in $MgCNi_3$.

The upper critical fields, $H_{c2}(T)$, determined from the specific heat data, are shown in Fig. 8. The $H_{c2}(T)$ data obtained from the specific heat are located in the small field range between the $H_{90}(T)$ and $H_{10}(T)$ curves determined from resistivity measurements (see Fig. 6).

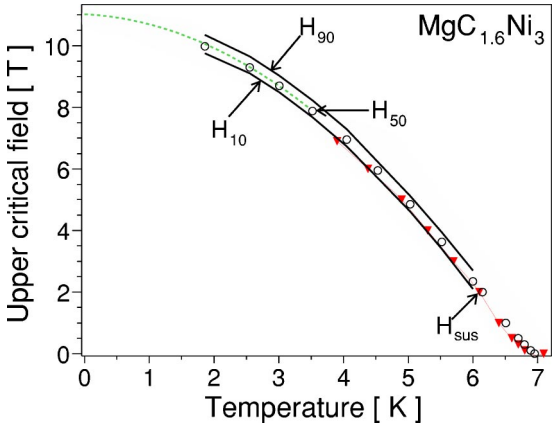

FIG. 7. (Color online) The upper critical field as a function of temperature. The circles show the midpoint of the transition (H_{50}). The two lines labeled H_{10} and H_{90} denote 10% and 90% of the normal-state resistivity. The triangles represent the upper critical field from susceptibility measurements (onset values). The dashed line illustrates the extrapolation of the resistivity data to $T=0$ K.

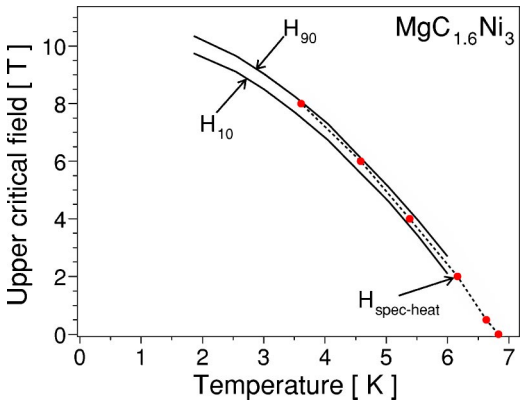

FIG. 8. (Color online) Comparison of upper critical field data determined from specific heat (●) and resistance measurements. H_{10} and H_{90} were determined at 10% and 90% of the normal-state resistivity, respectively. An entropy conserving construction was used to determine the upper critical field from the specific heat data of Fig. 5.

The extrapolation of $H_{90}(T)$ to $T=0$ K yields an upper critical field of $H_{c2}(0) \simeq 11.0$ T (see Fig. 7). The observed temperature dependence of the upper critical field is typical for $H_{c2}(T)$ data reported for $MgCNi_3$ so far[18] and was described[8,14,16] within the standard Werthammer-Helfand-Hohenberg (WHH) model[32] by conventional superconductivity. However, a quantitative analysis of H_{c2} data presented in Sec. VI A shows that the magnitude of the upper critical field $H_{c2}(0)$ at $T=0$ K can be understood only if strong electron-phonon coupling is taken into account.

V. ANALYSIS

A. Specific heat in the normal state

In order to describe the specific heat data in the normal state in an extended temperature range $T_c < T < 30$ K, the Debye low-temperature limit approximation for the lattice contribution [see Eq. (3)] was replaced by

$$c_{\text{lattice}}(T) = c_D(T) + c_E(T).$$

Here,

$$c_D(T) = \sum_{i=1}^{3} 3R\left(\frac{T}{\Theta_{Di}}\right)^3 \int_0^{\Theta_{Di}/T} dx \frac{e^x x^4}{(e^x - 1)^2}$$

stands for the Debye model[33,34] describing the three acoustic phonon branches, whereas the Einstein model[33,34]

$$c_E(T) = \sum_{i=4}^{15} R\left(\frac{\Theta_{Ei}}{T}\right)^2 \frac{\exp(\Theta_{Ei}/T)}{[\exp(\Theta_{Ei}/T) - 1]^2}$$

describes the 12 optical branches.

We found that the nine energetically lowest phonons (three acoustic and six optical modes) are sufficient to describe the normal-state specific heat up to $T=30$ K. To fit the model to the data, we started in the low-temperature region where the contribution of the Einstein-like modes are negligible and the specific heat is mainly determined by the

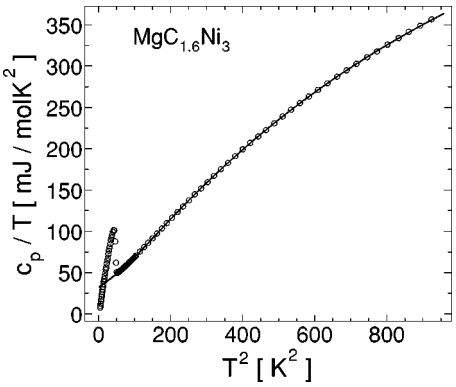

FIG. 9. Specific heat data $c_p(T)/T$ vs T^2 for zero magnetic field in the temperature range up to 30 K. The solid line is a fit of the lattice model (see text for details), showing very good agreement with the data for $T_c < T < 30$ K.

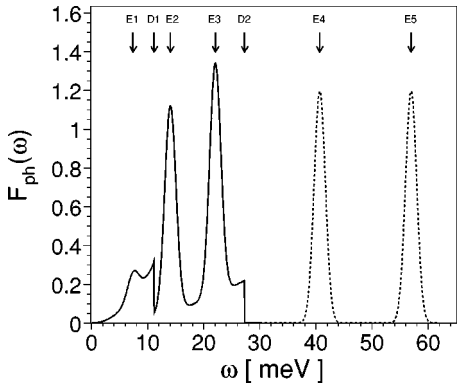

FIG. 10. Schematic phonon model spectrum $F_{ph}(\omega)$ for $MgC_{1.6}Ni_3$ derived from fit parameters according to Table I (dashed lines mark high-energy modes). The peak width of the optical modes was chosen arbitrarily as $\sigma_i^2 = 1$.

Debye-like modes. Starting parameters for the Sommerfeld parameter and the Debye temperature were taken from Sec. IV B. The contribution of the remaining Einstein modes was carefully estimated by stepwise increasing the temperature limit of the fit. The fitting procedure was performed using the ROOT program package.[35] It takes into account parameter correlations and non-linearities to calculate parameter errors. For the five parameters used, the standard deviations obtained from the least-squares fit amount to $\sigma \approx 0.1$ K for D1, D2, E1, and E2 and $\sigma \approx 10$ K for E3. The result of the fit is shown in Fig. 9. The Sommerfeld parameter converged to $\gamma_N^* = 31.4$ mJ/mol K^2, greater than determined from Fig. 5. Specific heat measurements up to $T = 300$ K on another piece from the initially prepared sample (which are not presented here) give the remaining six optical mode temperatures (where all other parameters were fixed). The obtained Debye and Einstein temperatures and the belonging grouping parameters ν_i are summarized in Table I. The phonon energies are in good agreement with recent calculations.[24]

The corresponding phonon spectrum has the form[34]

$$F_{\mathrm{ph}}(\omega) = 3\omega^2 \left[\nu_{\mathrm{D1}} \frac{\theta(\Omega_{\mathrm{D1}} - \omega)}{\Omega_{\mathrm{D1}}^3} + \nu_{\mathrm{D2}} \frac{\theta(\Omega_{\mathrm{D2}} - \omega)}{\Omega_{\mathrm{D2}}^3} \right] + \sum_{i=1}^{5} \frac{\nu_{\mathrm{E}i}}{\sqrt{2\pi\sigma_i^2}} \exp\left[-\frac{(\omega - \Omega_{\mathrm{E}i})^2}{2\sigma_i^2} \right],$$

where $\theta(x)$ is the well-known step function and Ω denotes the corresponding cutoff temperatures in meV. The result including higher optical modes is shown in Fig. 10. Our model parameters even reproduce the rather complex phonon dispersion along the Γ-X direction in the first Brillouin zone at low phonon energies, as can be seen from Fig. 11, where the used model is compared with calculations reported by Ignatov *et al.*[24] Even though our model only involves constant and linear dispersion by the Einstein and Debye models, respectively, the calculated phonon dispersion (right panel) is well reproduced (left panel), by means of superpositions of acoustic and optic phonon modes. The unusual low-temperature behavior of the Debye modes, seen in Fig.

TABLE I. Debye and Einstein temperatures with corresponding occupation numbers. Di denote the acoustic phonons and Ei the optical phonons. Θ gives the corresponding temperature and ν_i is the grouping parameter, giving the number of modes found to have the same temperature.

		Acoustic modes			Optical modes			
		D1	D2	E1	E2	E3	E4[a]	E5[a]
Θ	[K]	129	316	86	163	256	472	661
ν_i		1	2	0.33	2.67	3	3	3

[a]Derived from measurements up to $T = 300$ K.

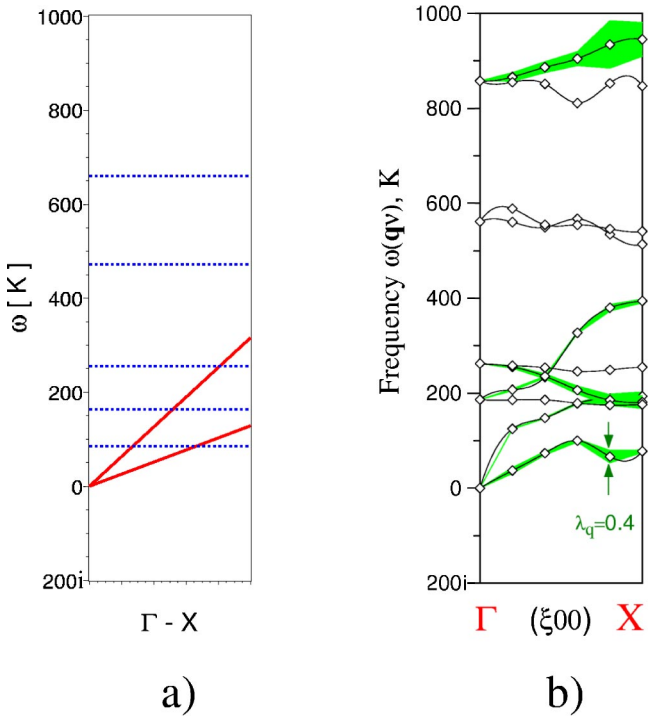

FIG. 11. (Color online) Phonon dispersion along the Γ-X direction in the first Brillouin zone. (a) Our model with acoustic phonons (solid lines) and optic phonons (dashed lines) according to Table I. (b) Calculations reported by Ignatov *et al.* after Ref. 24.

11(b), is simulated within our model by the degeneracy of the Einstein modes E1 and E2 [Fig. 11(a)]. The high-energy optic phonons obtained from the model are shifted to lower energies than predicted by the calculations. The shift is most probably caused by anharmonic effects, which usually increase specific heat data at higher temperatures.[24]

To investigate the electron-phonon coupling strength, the electron-phonon interaction function $\alpha^2F_{\mathrm{ph}}(\omega)$ is of interest. The coupling function $\alpha^2(\omega)$ is usually extracted from tunneling measurements. In the case of A15 compounds[36] and some borocarbides,[37] $\alpha^2(\omega)$ is found to be of the form $\alpha^2(\omega)=\delta/\sqrt{\omega}$, with a scaling parameter δ. Within this approach the logarithmically averaged mean phonon frequency $\omega_{\ln}$ was determined from

$$\omega_{\ln}=\exp\left(\frac{2}{\lambda_{\mathrm{ph}}}\int_0^\infty \mathrm{d}\omega\frac{\alpha^2(\omega)F(\omega)}{\omega}\ln\,\omega\right),$$

$$\lambda_{\mathrm{ph}}=2\int_0^\infty \mathrm{d}\omega\frac{\alpha^2(\omega)F(\omega)}{\omega} \tag{4}$$

as $\omega_{\ln}=143$ K. Note that shifting the high-energy modes to E4$\approx$580 K and E5$\approx$850 K, which would better reproduce the calculations from Ignatov *et al.*,[24] would shift $\omega_{\ln}$ to 140 K. This shows that these high-energy modes have a minor influence on the further analysis. $\omega_{\ln}$ is used in the well-known McMillan formula (refined by Allen and Dynes[38])

$$T_c\approx\frac{\omega_{\ln}}{1.2}\exp\left[-\frac{1+\lambda_{\mathrm{ph}}}{\lambda_{\mathrm{ph}}-\mu^*(1+0.6\lambda_{\mathrm{ph}})}\right] \tag{5}$$

to estimate the electron-phonon coupling constant λ_{ph}. Here μ^* denotes the usually weak Coulomb pseudopotential which has been chosen as $\mu^*=0.13$ in this case. With $T_c=6.8$ K the electron-phonon coupling constant amounts $\lambda_{\mathrm{ph}}=0.84$, suggesting moderate coupling as proposed, for instance, in Refs. 1 and 16. However, the low value of λ_{ph} estimated from Eq. (5) is in contradiction with our specific heat data as already mentioned in Sec. IV B. In particular, $\lambda_{\mathrm{ph}}=1.45$ was derived from the ratio γ_N^*/γ_0 and also the high value of the superconducting jump $\Delta c(T_c)/(\gamma_N T_c)=2.09$ indicates strong electron-phonon coupling. Strong electron-phonon coupling was also predicted by Ignatov *et al.*[24] ($\lambda_{\mathrm{ph}}=1.51$) on the basis of the calculations mentioned above.

In this context a more precise analysis of the low-temperature normal-state specific heat data is required. As can be seen from the dashed line in Fig. 12, the extended lattice model does not describe the magnetic field data. Even larger deviations are observed if the experimental data are described within the low-temperature limit of the Debye model (see Fig. 5). Lin *et al.*,[16] who found a similar upturn of the experimental data at low temperatures, tried to explain this behavior by the presence of Ni impurities. However, our x-ray analysis (see Fig. 3) shows no indication for Ni impurities in our sample. Recently, Shan *et al.*[18] found that the upturn mentioned can be easily reduced by lowering the carbon content. They attributed the observed upturn to some kind of boson mediated electron-electron interactions in

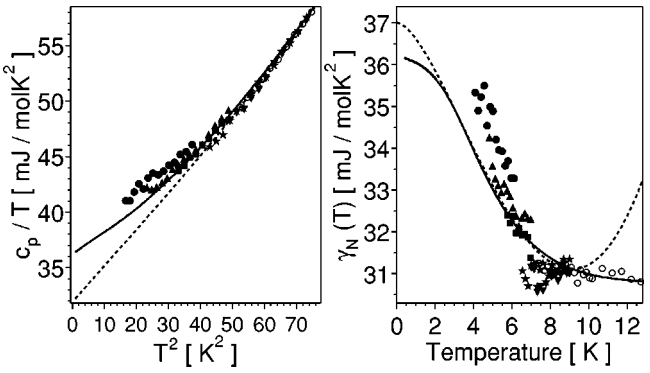

FIG. 12. Low-temperature normal state total and electronic specific heat including field measurements [0.5 T (▼), 2 T (★), 4 T (■), 6 T (▲), and 8 T (●)]. Left panel: specific heat data $c_p(T)/T$ vs T^2. Dotted line: extended lattice model describing the zero field data (see Fig. 9). Solid line: fit of the model (including lattice and paramagnon contribution) to the data. Right panel: electronic specific heat $\gamma_N(T)$ vs T in the normal state. Solid line: Sommerfeld parameter $\gamma_N(T)$ of the model (see text for details), describing the observed upturn of the specific heat at low temperatures. Dotted line: qualitative model for spin fluctuations according to Eq. (7).

MgC_xNi_3. This argument motivated us to search for other possible sources to explain the low-temperature upturn of the normal-state specific heat data.

The easiest explanation is an additional electron-boson interaction which may be (i) an electron-phonon interaction originating from additional phonon-softening of the lowest acoustic mode (suggested by Ignatov *et al.*[24] and verified experimentally by Heid *et al.*[39]) and/or (ii) an electron-paramagnon interaction (see Sec. I).

Specific heat measurements do not let one clearly distinguish between these possible origins, but since magnetization measurements on our sample (not presented here) show increasing spin fluctuations below $\sim$30 K in accordance with previous statements (see Sec. I), the focus in this paper lies on the electron-paramagnon interaction scenario. This is additionally supported by a small magnetic field dependence of the specific heat data, typically found in the presence of ferromagnetic spin fluctuations.

Within Eliashberg theory the renormalized normal-state specific heat is described by the temperature-dependent thermal mass $\Delta m^*(T)/m_{\mathrm{band}}$. Its contribution to the specific heat is given by

$$\Delta\gamma_{\mathrm{sf}}(T)=\frac{\Delta m^*(T)}{m_{\mathrm{band}}}\gamma_0,$$

with[40]

$$\frac{\Delta m^*(T)}{m_{\mathrm{band}}}=\frac{6}{\pi k_B T}\int_0^\infty \mathrm{d}\omega\alpha^2F(\omega)\{-z-2z^2\mathrm{Im}[\psi'(iz)]-z^3\mathrm{Re}[\psi''(iz)]\},$$

where $\psi(iz)$ is the digamma function and $z=\omega/(2\pi k_B T)$. The additional electron-paramagnon interaction function is of the form

$$\alpha^2 F_{sf} = a\omega\theta(\Omega_P - \omega) + \frac{b}{\omega^3}\theta(\omega - \Omega_P). \quad (6)$$

This model does not include the slight dependence on the applied magnetic field (which in addition can be temperature dependent). Therefore the parameters were chosen to give a consistent description of the low-temperature upturn on the one hand and the superconducting phase including the entropy conservation of the electronic specific heat in the superconducting state on the other hand (see Sec. V B). The chosen paramagnon-model temperature amounts to $\Omega_P \approx 2.15$ meV$\Rightarrow \Theta_P \approx 25$ K. The corresponding thermal mass $\Delta m^*(T=0)/m \approx 0.43$ is of the same order of magnitude as determined by Shan *et al.*[18] Since this low-energy excitation concerns the electronic part of the specific heat, we add it to the Sommerfeld parameter which then becomes temperature dependent. The electronic contribution to the specific heat increases from initially $\gamma_N^* = 31.4$ mJ/mol K^2 to $\gamma_N(0) = 36.0$ mJ/mol K^2. This is understandable since the paramagnon interaction dominates in the temperature range below 10 K. The solid line in Fig. 12 shows the good agreement of this extended model with the experimental data in the low-temperature region. In the following $\gamma_N(T)$ is denoted as γ_N for the sake of simplicity.

The usually applied model

$$\gamma_N \propto \delta T^2 \ln(T/T_0), \quad (7)$$

to describe spin fluctuation behavior, is shown in the right panel of Fig. 12 for comparison.

At this point the question of the strength of the coupling may be rechecked. Including the additional electron-paramagnon interaction, the Allen-Dynes formula, Eq. (5), becomes

$$T_c \approx \frac{\omega_{ln}}{1.2}\exp\left[-\frac{1+\lambda}{\lambda_{ph} - \lambda_{sf} - \mu^*(1+0.6\lambda)}\right], \quad (8)$$

with $\lambda = \lambda_{ph} + \lambda_{sf}$.[41,42] Using $\omega_{ln} = 143$ K, $T_c = 6.8$ K, $\mu^* = 0.13$, and $\lambda_{sf} = 0.43$, the electron-phonon coupling constant rises to $\lambda_{ph} = 1.91$. Using this value, the electron-phonon interaction function based on the approach $\alpha(\omega) = \delta/\sqrt{\omega}$ can now be determined by scaling the factor δ according to Eq. (4). The electron-boson interaction functions $\alpha^2 F_{ph}(\omega)$ and $\alpha^2 F_{sf}(\omega)$ are shown in Fig. 13.

The reliability of the model approach for the electron-phonon coupling function $\alpha(\omega) = \delta/\sqrt{\omega}$ can directly be checked from the band structure, using the ratio between the Sommerfeld parameter $\gamma_N(0) = 36.0$ mJ/mol K^2 and the free electron parameter $\gamma_0 = \pi^2 k_B^2 N(E_F)/3 = 11.0$ mJ/mol K^2:

$$\frac{\gamma_N(0)}{\gamma_0} = (1 + \lambda_{ph} + \lambda_{sf}). \quad (9)$$

With $\lambda_{sf} \approx 0.43$, the electron-phonon coupling constant becomes $\lambda_{ph} \approx 1.84$, showing good agreement between both approaches.

In the next section, the analysis of the specific heat in the normal state will be extended to the superconducting state.

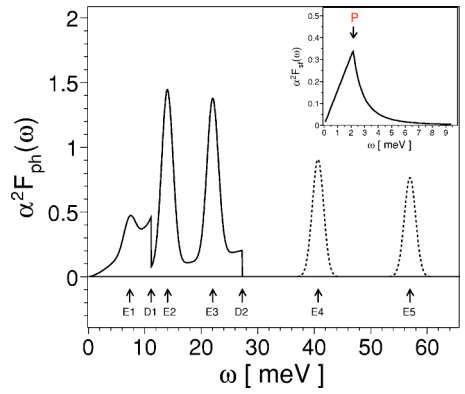

FIG. 13. (Color online) Electron-phonon interaction function $\alpha^2 F_{ph}(\omega)$ for $MgC_{1.6}Ni_3$. Phonon energies are marked by "E*i*" and "D*i*," respectively (see Fig. 10 and Table I). Inset: electron-paramagnon interaction function $\alpha^2 F_{sf}(\omega)$ according to Eq. (6). The paramagnon energy is marked by "P."

B. Specific heat in the superconducting state

Figure 14 shows the superconducting part of the electronic specific heat $\Delta c(T) = c_p(T) - c_n(T)$, obtained from the zero-field data. The superconducting transition temperature $T_c = 6.8$ K has been estimated by an entropy conserving construction (dashed line in Fig. 14). This value agrees well with the transition temperatures $T_c = 6.9$ K and $T_c = 7.0$ K, derived from resistance and from ac susceptibility data, respectively. The conservation of entropy, $\Delta S(T) = \int_0^{T_c} (\Delta c/T) dT$, is shown in the inset of Fig. 14. It was already mentioned that the high value of the jump, $\Delta c(T_c)/(\gamma_N T_c) = 2.09$, found for the investigated sample can be explained by strong electron-phonon coupling. Nevertheless, we will start to analyze $\Delta c(T)$ for $T < T_c/2$ within the BCS theory, since the deviation from the weak coupling temperature dependence of the gap is mainly restricted to the vicinity of the jump. The temperature dependence of $\Delta c(T) = c_p(T) - c_n(T)$ in the weak coupling BCS theory ($T_c \ll \omega_{ln}$) is given by an approximative formula

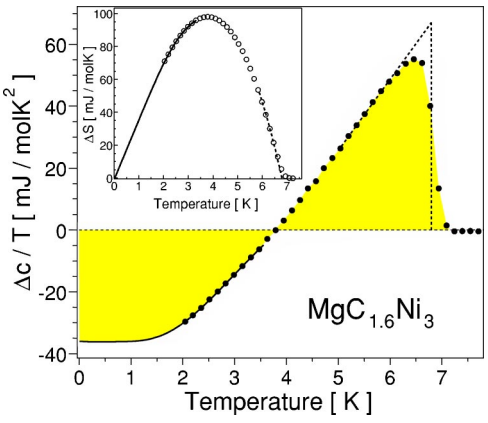

FIG. 14. (Color online) Electronic specific heat data $\Delta c/T$ vs T in the superconducting state (solid circles). The solid line in the temperature range $0 < T < 3.4$ K corresponds to Eq. (10). Dotted line: entropy conserving construction to get the idealized jump. Inset: entropy conservation for the electronic specific heat in the temperature range $0 < T < T_c$.

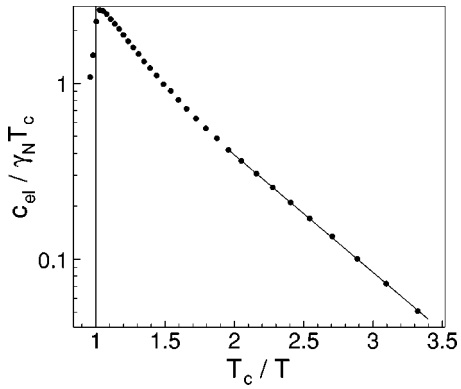

FIG. 15. Normalized electronic specific heat contribution vs T_c/T. The solid line is a fit of Eq. (11) to the experimental data.

$$\Delta c(T) = 8.5\gamma_N T_c \exp\left(-0.82\frac{\Delta_{BCS}(0)}{k_B T}\right) - \gamma_N T, \quad (10)$$

valid in the temperature range of $2 < T_c/T < 6$ corresponding in this case to 1 K $< T <$ 3.4 K. Equation (10) can be fitted to the data by using the phenomenological gap $2\Delta_{exp}/k_B T_c = 3.75$, slightly exceeding the BCS weak coupling prediction $2\Delta_{BCS}(0)/k_B T_c = 3.52$. The fit, which is shown as the solid line in Fig. 14, describes the experimental data in the range of 2 K $< T <$ 3.5 K quite well.

To examine the temperature dependence of the electronic specific heat,

$$c_{el} = c_p(T) - c_{lattice}(T) = \Delta c(T) + \gamma_N T_c,$$

at $H=0$ in detail, $c_{el}(T)/\gamma_N T_c$ is plotted logarithmically versus T_c/T (Fig. 15). The corresponding formula to Eq. (10) reads

$$\frac{c_{el}(T)}{\gamma_N T_c} = 8.5\ \exp\left(-0.82\frac{\Delta_{exp}}{k_B T}\right), \quad (11)$$

if $\Delta_{BCS}(0)$ is replaced by Δ_{exp}. The solid line in Fig. 15 is a fit of Eq. (11) to the experimental data, which show an exponential temperature dependence at low temperatures ($T_c/T \geqslant 2$). This is a strong indication for *s*-wave superconductivity in $MgC_{1.6}Ni_3$.

The discrepancy between the values of the experimentally found and the BCS gap as well as the strongly enhanced specific heat jump $\Delta c(T_c)$ are clear indications of strong electron-phonon coupling which is in accordance with our normal-state specific heat analysis. Thus it is now straightforward to investigate the electron-phonon coupling strength and thus the characteristic phonon frequency ω_{ln}, introduced in Sec. V A, from the superconducting state characteristics. The Eliashberg theory provides the following approximate formulas, which includes strong coupling corrections within an isotropic single-band model and links $x = \omega_{ln}/T_c$ to experimental thermodynamic quantities:[22]

$$\frac{2\Delta(0)}{k_B T_c} = 3.53 B_0(x), \quad (12a)$$

$$\frac{\Delta c(T_c)}{\gamma_N T_c} = 1.43 B_1(x), \quad (12b)$$

$$\frac{\Delta c(T) - \Delta c(T_c)}{\gamma_N T_c - \gamma_N T} = -3.77 B_2(x), \quad (12c)$$

$$\frac{\gamma_N T_c^2}{H_c^2(0)} = 0.168 B_3(x), \quad (12d)$$

$$-\frac{H_c(0)}{\left.\frac{dH_c}{dT}\right|_{T_c} T_c} = 0.576 B_4(x). \quad (12e)$$

The corresponding logarithmic correction terms are given by

$$B_0(x) = 1 + 12.5 x^{-2} \ln\frac{x}{2}, \quad (13a)$$

$$B_1(x) = 1 + 53 x^{-2} \ln\frac{x}{3}, \quad (13b)$$

$$B_2(x) = 1 + 117 x^{-2} \ln\frac{x}{2.9}, \quad (13c)$$

$$B_3(x) = 1 - 12.2 x^{-2} \ln\frac{x}{3}, \quad (13d)$$

$$B_4(x) = 1 - 13.4 x^{-2} \ln\frac{x}{3.5}. \quad (13e)$$

Now, using Eq. (12a), $T_c = 6.8$ K, and the gap value $\Delta_{exp}(2\text{ K}) = 1.10$ meV, one arrives at $\omega_{ln} = 149$ K.

Using the value of the idealized jump of the specific heat, $\Delta c(T_c)/(\gamma_N T_c) = 2.09$ in Eq. (12b) with $T_c = 6.8$ K, $\omega_{ln} = 88$ K is derived.

Comparing the linear slope of the idealized specific heat in the superconducting state of −6.7, obtained from Fig. 14 with Eq. (12c), one gets $\omega_{ln} = 109$ K.

In view of strong coupling effects the ratio $\gamma_N T_c^2/H_c^2(0)$, implying again only thermodynamic quantities, is of interest. Known superconductors show values between 0.17 and 0.12 ranging from weak to strong coupling, respectively (see, for example, Ref. 22, p. 1086). The thermodynamic critical field $H_c(T)$ can be determined with the help of the Gibbs free energy $dF = -SdT - MdB$ as

$$H_c(T) = \sqrt{-8\pi\Delta F}. \quad (14)$$

ΔF is to be extracted from the specific heat in the superconducting state, $\Delta c(T) = -T d^2(\Delta F)/dT^2$. The temperature dependence of $H_c(T)$ is shown in Fig. 16. With $H_c(0) = 179.6$ mT we found $\gamma_N T_c^2/H_c^2(0) = 0.155$. From Eq. (12d) we get $\omega_{ln} = 110$ K (with $T_c = 6.8$ K).

Next, from the derivative of the thermodynamic critical field at zero temperature, dH_c/dT, the ratio $H_c(0)/[dH_c(T)/dT|_{T_c} T_c]$ can be estimated. The value at $T = T_c$ (of the idealized jump construction) amounts to

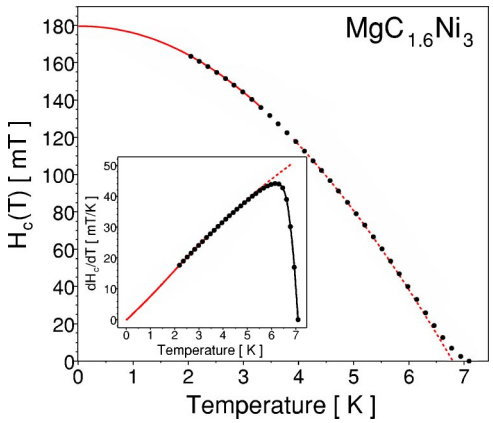

FIG. 16. (Color online) Temperature dependence of the thermodynamic critical field $H_c(T)$ (solid circles) derived from the electronic specific heat in the superconducting state using Eq. (14). Solid line ($0<T<3.4$ K): single-band model according to Eq. (11). Dotted line: idealized jump construction (see Fig. 15). Inset: derivative dH_c/dT vs T (solid circles) and idealized jump (dotted line).

$dH_c(T)/dT|_{T_c}=50.236$ (see the dashed line in the inset of Fig. 16). Using the experimental value of $H_c(0)/[dH_c(T)/dT|_{T_c}T_c]=0.525$ in Eq. (12e), a value of $\omega_{ln}=102$ K is extracted.

It should be noted that Eqs. (12a) and (12e) can be used to estimate the value of the gap $\Delta(0)$ from the thermodynamic critical field $H_c(0)$, due to similar dependences on strong coupling corrections:[43]

$$\left(\frac{T}{H_c(0)}\frac{dH_c(T)}{dT}\right)\bigg|_{T=T_c} \approx \frac{\Delta(0)}{k_B T_c}.$$

Using $dH_c(T)/dT|_{T_c}=50.236$, we get $2\Delta(0)/k_BT_c\approx 3.80$, agreeing well with the single-band result $2\Delta_{exp}/k_BT_c=3.75$ of Eq. (11).

In summary, ω_{ln} was estimated from five different thermodynamic relations, only involving experimental results. The mean value $\overline{\omega_{ln}}=(111\pm23)$ K is in good agreement with calculations of Ignativ *et al.*[24] An overview of the results is given in Fig. 17. Note that a similar analysis was already successfully used to describe some borocarbide superconductors.[37,44]

The mean value $\overline{\omega_{ln}}$, derived from the superconducting state is somewhat smaller than the normal-state result, $\omega_{ln}=143$ K. This may be attributed to an additional phonon softening contribution or the approximative approach of the electron-phonon coupling function $\alpha^2(\omega)$ (see Sec. V A). Nevertheless, by checking Eq. (8) with $\overline{\omega_{ln}}=(111\pm23)$ K, $T_c=6.8$ K, $\mu^*=0.13$, and $\lambda_{sf}=0.43$ the electron-phonon coupling constant becomes $\lambda_{ph}=1.95-2.38$, whereas $\lambda_{ph}=1.91$ was derived from $\omega_{ln}=143$ K for the same parameters. It should be noted here that Eqs. (12) were derived assuming a small value for the Coulomb pseudopotential μ^*, which is oversimplified considering enhanced electron-paramagnon coupling found in this analysis. A rough correction would shift the characteristic phonon frequency ω_{ln} to slightly

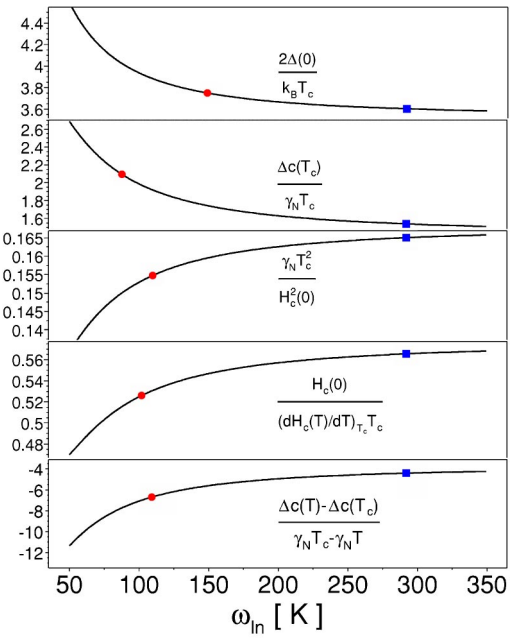

FIG. 17. (Color online) Several thermodynamic quantities in dependence on the characteristic phonon frequency ω_{ln} according to Eqs. (12) and (13). Solid circles: thermodynamic quantities estimated for $MgC_{1.6}Ni_3$ from experimental data. Strong discrepancies are found within the low-temperature Debye limit (solid squares). Note that the weak coupling limit is reached in the asymptotic extrapolation $\omega_{ln}\to\infty$.

higher values and a coupling constant of $\lambda_{ph}\approx 1.9$ seems to be most likely.

The analysis of the thermodynamic properties of $MgCNi_3$ presented so far clearly points to strong electron-phonon coupling. However, the temperature dependence of the thermodynamic critical field $H_c(T)$ shown in Fig. 16 strongly deviates from analogous data for well-known strong coupling superconductors such as Hg or Pb. $H_c(T)$ is usually analyzed in terms of the deviation function $D(t)=H_c(T)/H_c(0)-(1-t^2)$ with $t=T/T_c$. The deviation function of the above-mentioned strong coupling superconductors is positive and goes through a maximum at $t^2\approx 0.5$. The deviation function of $MgCNi_3$ is shown in Fig. 18. Instead of the expected positive sign, $D(t^2)$ of $MgCNi_3$ becomes negative already above about $0.3T_c$. The shape of the deviation function of $MgCNi_3$ closely resembles that one of Nb having an electron-phonon coupling strength of $\lambda_{ph}\approx 1.0$. We remind the reader that the weak coupling BCS model yields a negative maximum deviation of $\approx 3.8\%$ (see Fig. 18). Thus, at first glance, our result seems to be in contradiction with the strong electron-phonon coupling suggested above. It turns out that this contradiction can be resolved, taking into account a splitting of the electron-phonon interaction function into a high and a low (soft) energy part. This is illustrated in Fig. 19, where a two-phonon peak spectrum with equal coupling strengths of both peaks located at ω_1 and ω_2 has been analyzed in the strong coupling case of $\lambda_{ph}\approx 2$ under consideration. The theoretical curves calculated within the ISB are shown for different frequency ratios ω_1/ω_2. For $\omega_1/\omega_2\approx 8$, the "standard" strong coupling behavior—namely, a positive

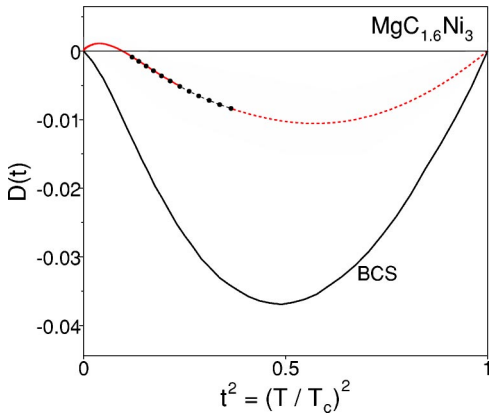

FIG. 18. (Color online) Deviation function of the thermodynamic critical field of $MgC_{1.6}Ni_3$ (solid circles) as function of $(T/T_c)^2$. The solid line for $0<T<0.34$ K corresponds to Eq. (11); the dotted line corresponds to the idealized jump construction (see Fig. 14). For comparison, the weak coupling BCS (Ref. 45) is shown.

deviation function—is completely removed and the deviation function becomes negative. Considering the low-energy modes E1 and D1, found in the analysis of the specific heat in the normal state (see Figs. 10 and 13), this situation is easily imaginable to be valid in the case of $MgCNi_3$.

In the superconducting state a linear-in-T electronic specific heat contribution $\gamma(H)T$ arises from the normal conducting cores of the flux lines for applied magnetic fields $H>H_{c1}$.

This contribution can be expressed as $\gamma(H)T=c_p(T,H)-c_p(T,0)$,[46] where $c_p(T,0)$ is the specific heat in the Meissner state. Specific heat data for $MgC_{1.6}Ni_3$ at $T=2$ K were analyzed in order to derive the field dependence of $\gamma(H)$. In Fig. 20, the obtained $\gamma(H)/\gamma_N$ is plotted against $H/H_{c2}(0)$ using $H_{c2}(0)=11.0$ T.

The field data of c_p/T shown in Fig. 20 can be described in accord with results from Ref. 16 by the expression γ/γ_N

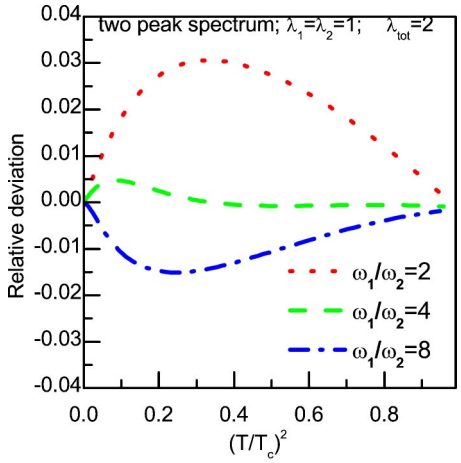

FIG. 19. (Color online) Normalized deviation function calculated within the Eliashberg theory for an idealized two-peak phonon spectrum located at ω_1 and ω_2 with equal electron-phonon coupling parameters $\lambda_1=\lambda_2=1$ and strong total coupling parameter of $\lambda_{ph,tot}=2$. Shown are results for $\omega_1/\omega_2=2$, 4, and 8.

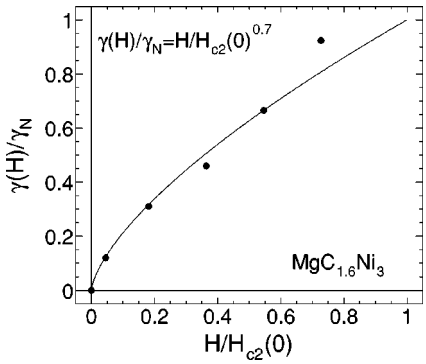

FIG. 20. Normalized field-dependent Sommerfeld parameter $\gamma(H)/\gamma_N$ plotted against $H/H_{c2}(0)$. Solid circles: $\gamma(H)/\gamma_N=[c_p(T,H)-c_p(T,0)]/\gamma_N$ at $T=2$ K for different applied magnetic fields. The solid line is a fit of $\gamma(H)/\gamma_N=[H/H_{c2}(0)]^{0.7}$ using $H_{c2}(0)=11$ T and γ_N at $T=2$ K.

$=[H/H_{c2}(0)]^{0.7}$ which differs from the linear $\gamma(H)$ law expected for isotropic s-wave superconductors in the dirty limit.

A nonlinear field dependence close to $\gamma(H)\propto H^{0.5}$ has been reported for some unconventional superconductors with gap nodes in the quasiparticle spectrum of the vortex state as $YBa_2Cu_3O_7$ (Ref. 47) and in the heavy fermion superconductor UPt_3 (Ref. 48), but also in some clean s-wave superconductors as $CeRu_2$ (Ref. 49), $NbSe_2$ (Refs. 46 and 50), and the borocarbides RNi_2B_2C ($R=Y,Lu$) (Refs. 51 and 52). Delocalized quasiparticle states around the vortex cores, similar as in d-wave superconductors, seem to be responsible for the nonlinear $\gamma(H)$ dependence in the borocarbides.[53,54]

C. Main superconducting and thermodynamic parameters

In this subsection we collect the values of the main physical parameters we have found experimentally and compare them with available data in the literature. In order to make this comparison as complete as possible we estimate (calculate), from our data and from those of Ref. 14, the lower critical field $H_{c1}(0)$ and the penetration depth $\lambda_L(0)$ at zero temperature adopting the applicability of the standard Ginzburg-Landau (GL) theory. Within this theory the penetration depth is given by the relation

$$\lambda_L(0)=\kappa(0)\xi_{GL}(0), \tag{15}$$

where the Ginzburg-Landau coherence length $\xi_{GL}(0)$ and the Ginzburg-Landau parameter κ are related to the upper and the thermodynamic critical fields as

$$\xi_{GL}(0)=\sqrt{\Phi_0/2\pi H_{c2}(0)},$$

$$\kappa(0)=\frac{H_{c2}(0)}{\sqrt{2}H_c(0)},$$

with the flux quantum Φ_0. With $H_{c2}(0)=11$ T and $H_c(0)=180$ mT (see Sec. V B), $\xi_{GL}(0)=5.47$ nm and $\kappa(0)=43.3$ are obtained. Using theses values in Eq. (15), the penetration depth is estimated to be $\lambda_L(0)=237$ nm. Our calculated value

TABLE II. Main superconducting and thermodynamic electronic parameters for $MgCNi_3$.

		Present work[a]	Ref. 55[a]	Ref. 14[b]	Ref. 56[b]
T_c	[K]	6.8	6.4	7.63	7.3
$H_{c2}(0)$	[T]	11	11.5	14.4	16
$H_c(0)$	[T]	0.18	0.29 ± 0.04	0.19	0.22[f]
$H_{c1}(0)$	[mT]	11.3[c]	23 ± 7[c]	10.0[c]	12.6[d]
$\xi_{GL}(0)$	[nm]	5.47	5.3	4.8	4.5
$\kappa(0)$		43.3	29.0 ± 5.0	54.0	51
$\lambda_L(0)$	[nm]	237[c]	154 ± 26[d]	248[c]	230.0[c]
γ_N	[mJ/mol K^2]	31.4	33.6	30.1	
$\Delta c/\gamma_N T_c$		2.09	1.97	2.1	
Θ_D^*	[K]	292	287	284	
ω_{ln}	[K]	143	135[e]	161[e]	

[a]Using a parabolically extrapolated $H_{c2}(0)$ value.
[b]Adopting the WHH (dirty limit) estimate for $H_{c2}(0)$.
[c]Calculated.
[d]Measured.
[e]Calculated [Eq. (8) using $\lambda_{ph}=1.85$, $\lambda_{sf}=0.43$, $\mu^*=0.13$].
[f]Recalculated instead of 0.6 T in Ref. 56.

agrees well with measurements performed by Prozorov *et al.*[20] resulting in $\lambda_L(0)=(250\pm20)$ nm. It should be noted that Lin *et al.*[16] measured a penetration depth of $\lambda_L(0)=(128-180)$ nm for their sample (see also Ref. 55); possible consequences will be discussed in Sec. VI A. To complete the critical field analysis, the lower critical field $H_{c1}(0)$ can be estimated using

$$H_{c1}(0)H_{c2}(0)=H_c^2(0)[\ln\kappa(0)+0.08].$$

With $H_{c2}(0)=11$ T and $\kappa(0)=43.3$ we get $H_{c1}(0)=11.3$ mT, agreeing well with $H_{c1}(0)=12.6$ mT, measured by Jin *et al.*[56] The results are shown in Table II, where for comparison results of Refs. 14, 55, and 56 have been included. Comparing these sets one finds a general qualitative accord.

VI. THEORETICAL ANALYSIS AND DISCUSSION

Naturally, any microscopic parameter set containing various coupling constants, etc., to reproduce the measured quantities reported above is strongly model dependent. In this context even the case of relatively simple Fermi surfaces provides a difficult task to solve the full three- (four-) dimensional Eliashberg problem with a given $v_F(\vec{k})$ and $\alpha^2F(\vec{k},\vec{k}',\omega)$ for all physical quantities of interest. However, the solution of this problem can be sufficiently simplified for three practically important cases: (i) the relatively simple standard ISB model, where $v_F(\vec{k})$ is constant and the spectral function α^2F depends only on the boson (phonon) frequency, (ii) a separable anisotropic single-band model which exploits the so-called first-order Fermi surface harmonic approximation, and (iii) the isotropic two-band (ITB) model.

Due to the present lack of single-crystal samples, we will ignore the second issue, completely.

The ITB model is a straightforward generalization of the ISB with respect to two coupling constants and two order parameters, two Fermi velocities, two partial densities of states, two intraband and one interband scattering rate(s), etc. In particular, the different order parameters may be important for the specific heat and related properties whereas the upper critical field and the penetration depth are affected also by the different Fermi velocities (see below). Multiband (two-band) (and similar anisotropy) effects for several physical properties in the superconducting state have been in principle well known for a long time,[57] especially for weakly coupled superconductors in the clean limit. To the best of our knowledge, their interplay with disorder and strong coupling effects is less systematically studied. In particular this is caused by the increased number of input parameters and the necessity of a large amount of numerical calculations.

Most experimental quantities of $MgCNi_3$ are consistently described within an ISB model. From the specific heat alone, there is no conclusive evidence for the need of an ITB approach; thus, we focus mainly on the ISB model. However, in view of thermopower[10] and Hall data,[8,15] which cannot be described within the ISB model intrinsically, the ITB model deserves more attention. Therefore, in the end of this section, we will briefly mention to which extent the ITB model modifies the derived results. The interested reader is referred to a more detailed analysis, which is partly shown in Ref. 58 and will be published elsewhere.

A. Isotropic single-band analysis

In the following section the electron-phonon coupling strength λ_{ph} is extracted from a simultaneous analysis of the upper critical field and the penetration depth in terms of the unknown impurity scattering rate γ_{imp}[K]. Since the specific heat measurements do not clearly characterize $MgCNi_3$ as a one-band or multiband superconductor, the analysis starts within an ISB model. Within this model the upper critical field $H_{c2}(0)$ is given by[59]

$$H_{c2}(0)[\mathrm{T}] = H_{c2}^{\mathrm{cl}}(0)\left[1 + \frac{0.13\gamma_{\mathrm{imp}}[\mathrm{K}]}{T_c(1+\lambda_{\mathrm{ph}})}\right], \tag{16}$$

where

$$H_{c2}^{\mathrm{cl}}(0)[\mathrm{T}] = 0.0237\frac{(1+\lambda_{\mathrm{ph}})^{2.2}T_c^2[\mathrm{K}]}{v_F^2[10^5\ \mathrm{m/s}]}, \tag{17}$$

and $\gamma_{\mathrm{imp}} = v_F/l_{\mathrm{imp}}$ is the scattering rate which determines the intrinsic resistivity (l_{imp} denotes the corresponding mean free path and v_F the effective Fermi velocity). The London penetration depth including the unknown impurity scattering rate γ_{imp} is given by an approximative formula

$$\lambda_L(0) \approx \tilde{\lambda}_L(0)\sqrt{(1+\lambda_{\mathrm{ph}})\left(1 + 0.7\frac{\gamma_{\mathrm{imp}}}{2\Delta_{\mathrm{exp}}}\right)}$$
$$\equiv \tilde{\lambda}_L(0)\sqrt{(1+\lambda_{\mathrm{ph}})\left(1 + 0.7\frac{\gamma_{\mathrm{imp}}}{T_c}\frac{T_c}{2\Delta_{\mathrm{exp}}}\right)}, \tag{18}$$

valid for $\lambda_{\mathrm{ph}} < 2.5$ (see the Appendix for the exact numerical expression), with the bare clean limit London penetration depth

$$\tilde{\lambda}_L(0) = \frac{c}{\omega_{\mathrm{pl}}} \approx \frac{197.3\ \mathrm{nm}}{\omega_{\mathrm{pl}}[\mathrm{eV}]}. \tag{19}$$

Using Eqs. (16) and (18), $\gamma_N^* = \gamma_0(1+\lambda_{\mathrm{ph}})$, and the experimentally determined quantities from Table II, we now will check the applicability of the ISB model. For this aim we consider the ratio

$$R = \frac{6.77\times10^{-3}\times\gamma_N^*[\mathrm{mJ/mol\ K^2}]\times\lambda_L^2(0)[\mathrm{nm^2}]\times T_c^2[\mathrm{K^2}]}{H_{c2}(0)[\mathrm{T}]\times V[\mathrm{nm^3}]}, \tag{20}$$

which includes the values of six experimentally readily accessible quantities: the Sommerfeld coefficient γ_N^*, $H_{c2}(0)$, T_c, $\lambda_L(0)$, and the volume of the unit cell. The dependence of R on the parameter $\gamma_{\mathrm{imp}}/T_c$ can be expressed as

$$R = \frac{1 + 0.35\gamma_{\mathrm{imp}}/\Delta(0)}{(1+\lambda_{\mathrm{ph}})^{0.2}\{1 + 0.13\gamma_{\mathrm{imp}}/[T_c(1+\lambda_{\mathrm{ph}})]\}}. \tag{21}$$

In Fig. 21, the theoretical $R(\gamma_{\mathrm{imp}}/T_c)$ curves obtained from Eq. (21) for several λ_{ph} values are compared with the value of R derived from our experimental data which is represented in Fig. 21 as a horizontal line. Crossing points between the theoretical prediction and the experimental result, which confirm the applicability of the ISB, are found for $\lambda_{\mathrm{ph}} \geqslant 0.8$ at low scattering rates. Even in the case of higher electron-phonon coupling constants of $\lambda_{\mathrm{ph}} \approx 2$, a clean limit scenario with $\gamma_{\mathrm{imp}}/T_c \approx 1$ is favored within the ISB analysis. The dirty limit (with weak or medium coupling) as proposed in Ref. 16 can be excluded from the R check in Fig. 21. In this context it is interesting to compare the $H_{c2}(0)$ data of sintered samples with those of low-resistivity films reported by Young *et al.*[15] From $H_{c2}(0) = 12.8$ T in this case, $\xi_{GL}(0) = 4.5$ nm is derived, far exceeding the mean free path $l_{\mathrm{imp}} = 0.14$ nm, estimated from their ρ_0 (see Sec. IV A). Consequently, one would classify these films to be in the extreme dirty limit. However, since T_c and $H_{c2}(0)$ are comparable

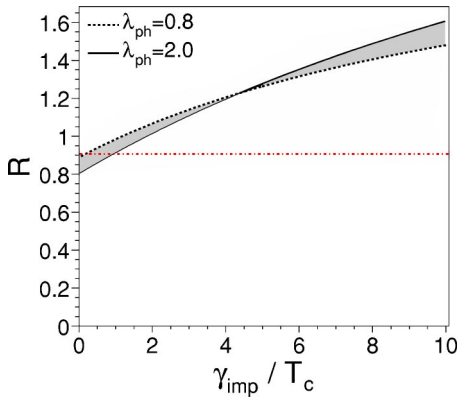

FIG. 21. (Color online) Parameter R vs $\gamma_{\mathrm{imp}}/T_c$ according to Eq. (21) in the range of electron-phonon coupling constants $0.8 \leqslant \lambda_{\mathrm{ph}} \leqslant 2.0$. Horizontal dash-dotted line: experimental result for $MgC_{1.6}Ni_3$ derived from Eq. (20).

with results of the sintered samples (see Table II), it can be concluded that for the thin film samples, like in the case of sintered samples, the measured residual resistivity is not intrinsic. Hence, these films are expected to be also near to the clean limit. From this point of view, neutron-irradiated samples reported by Karkin *et al.* are most interesting.[60]

It is noteworthy that the proposed R check is much more convenient than the similar Q check, proposed recently by two of the present authors,[59] since the dependence on λ_{ph} is considerably weaker for R and, which is more important, R does not depend on the band structure calculation. Thus comparing the results derived above with the expectations from these calculations, additional information on the nature of superconductivity in $MgCNi_3$ may be extracted. From Eqs. (16) and (17), the effective Fermi velocity (in 10^7 cm/s)

$$v_F = 0.154(1+\lambda_{\mathrm{ph}})^{1.1}T_c[\mathrm{K}]$$
$$\times\sqrt{\frac{1 + 0.13\gamma_{\mathrm{imp}}[\mathrm{K}]/[T_c[\mathrm{K}](1+\lambda_{\mathrm{ph}})]}{H_{c2}(0)[\mathrm{T}]}} \tag{22}$$

is obtained. Using the very weak scattering rates $\gamma_{\mathrm{imp}}/T_c \leqslant 1$ derived above and the experimental values $H_{c2}(0) = 11$ T and $T_c = 6.8$ K, one estimates from Eq. (22) $v_F \approx (0.60-1.08)\times10^7$ cm/s for electron-phonon coupling constants in the range of $0.8 \leqslant \lambda_{\mathrm{ph}} \leqslant 2.0$. Comparing this result with our band structure calculations (see Sec. II), one realizes consistence with the averaged $v_{\mathrm{hc2,h}} = 1.07\times10^7$ cm/s from the two-hole Fermi surface sheets (Sec. II) for strong electron-phonon coupling of $\lambda_{\mathrm{ph}} \approx 2.0$. Thus, the relatively high value of the upper critical field of $H_{c2}(0) = 11$ T can be attributed to strong electron-phonon coupling for the hole subsystem. The second electron band plays a minor role for $H_{c2}(0)$ due to its much faster Fermi velocities and the much lower partial density of states.

Having adopted the dominant hole picture, we also can start from the band structure results, using the Fermi velocity $v_{F,h}$ and the plasma frequency $\omega_{\mathrm{pl,h}}$ of the hole band. Then we have to find consistent values of $\lambda_{\mathrm{ph,h}}$ and γ_{imp}, which describe the $H_{c2}(0)$ and $\lambda_L(0)$ data.

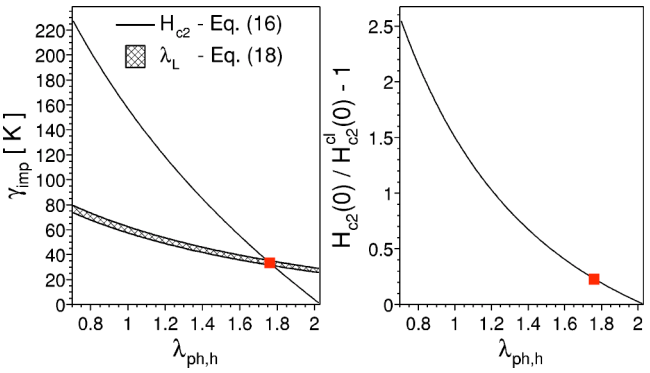

FIG. 22. (Color online) Left panel: correlation between impurity scattering rate γ_{imp} and electron-phonon coupling constant $\lambda_{ph,h}$ derived from Eqs. (16) and (18) using $H_{c2}(0)=11$ T, $T_c=6.8$ K, $v_F=1.07\times10^7$ cm/s, $\lambda_L(0)=237$ nm, and $2\Delta(0)\approx2.2$ meV. The point of intersection of both curves marked by a solid square points to an electron-phonon coupling constant of $\lambda_{ph,h}=1.74-1.78$ in the investigated $MgC_{1.6}Ni_3$ sample. Right panel: ratio $([H_{c2}(0)/H_{c2}^{cl}(0)]-1)$ plotted against $\lambda_{ph,h}$. The solid square again corresponds to $\lambda_{ph,h}=1.74-1.78$. From $H_{c2}(0)=11$ T one estimates $H_{c2}^{cl}(0)\approx(8.79-9.07)$ T for the upper critical field in the clean limit.

From the plasma frequency of band 1, $\hbar\omega_{pl,1}=1.89-1.94$ eV (see Sec. II), we get $\tilde{\lambda}_L(0)=(101.7-104.4)$ nm, using Eq. (19). With the empirical values of $\lambda_L(0)=237$ nm and $2\Delta(0)\approx2\Delta_{exp}=2.2$ meV $\doteq25.5$ K for the superconducting gap (see Sec. V B), Eq. (18) depends only on γ_{imp} and $\lambda_{ph,h}$ (of the hole band). The same applies to Eq. (16), using the experimental values $H_{c2}(0)=11$ T, $T_c=6.8$ K and the calculated average Fermi velocity of the hole band, $v_{hc2,h}=1.07\times10^7$ cm/s. The correlation between γ_{imp} and $\lambda_{ph,h}$, emerging from these two equations, is shown in the left panel of Fig. 22. The intersection of both graphs gives $\lambda_{ph,h}=1.74-1.78$ and $\gamma_{imp}=(31.0-36.0)$ K. Thus, we arrive at a higher, more realistic scattering rate compared with $\gamma_{imp}\approx T_c$ obtained from the R check in Fig. 21. The corresponding ratio $([H_{c2}(0)/H_{c2}^{cl}(0)]-1)$, giving the deviation of $H_{c2}(0)$ from the clean limit value $H_{c2}^{cl}(0)$, is plotted in the right panel of Fig. 22. One gets $H_{c2}^{cl}(0)\approx(8.79-9.07)$ T.

To summarize this part, already in the simplest possible approach two general properties of $MgCNi_3$ are derived: (i) strong electron-phonon coupling and (ii) intrinsic clean limit at least for the hole subsystem.

Nevertheless, it should be noted that recent preliminary measurements of the penetration depth by Lin *et al.*,[16] resulting in $\lambda_L(0)=(128-180)$ nm, are not compatible with the presented effective single-band analysis (see also Ref. 55). Especially the R check [Eqs. (20) and (21)] results in unphysical solutions ($\lambda_{ph}=30$ as a lower limit), using the values presented in Refs. 16 and 55 (see as well Table II). The consequences, if these measurements could be verified, remain unclear.

As stated above, the contribution of the second band is expected to be small due to the much smaller partial density of states. Nevertheless, it is necessary to check its influence on the penetration depth to estimate an error of the derived

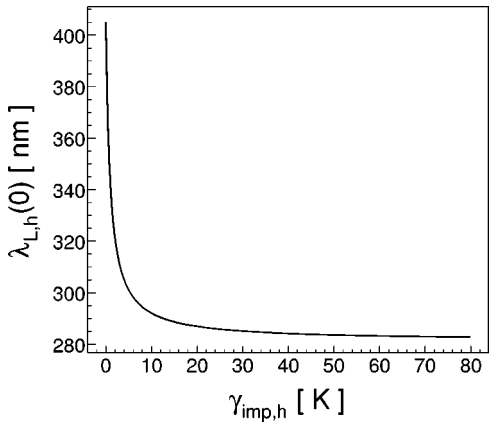

FIG. 23. Penetration depth at zero temperature vs scattering rate in the hole band, using $\gamma_{imp,el}/\gamma_{imp,h}\approx4.81$ from Eq. (1).

coupling constant $\lambda_{ph,h}$. Using a two-band approach, the penetration depth attributed to the hole band is found to be reduced compared to the value derived from Eq. (15). The result is plotted in Fig. 23. From this analysis we estimate an error of about $\approx10\%$ for $\lambda_{ph,h}$ (see Ref. 58 for the detailed analysis).

B. Strong coupling and enhanced depairing

Several results of our analysis of the experimental data are summarized in Table III. The comparison of the estimated λ_{ph} values clearly points to strong electron-phonon coupling. Nevertheless, the strong coupling scenario realized in $MgCNi_3$ has been questioned.[1,16] The strong electron-phonon coupling found for $MgCNi_3$ requires a sizable depairing contribution to explain the low T_c value; otherwise, at least a twice as large T_c would be expected. It is illustrative to compare different approaches for the calculation of T_c to analyze the electron-phonon coupling strength under consideration of the low-temperature upturn of the specific heat in the normal state (see Sec. V A).

In a first approach usually the low-temperature Debye approximation is used to extract the Debye temperature which we did in Sec. IV B for comparison. Our result of $\Theta_D^*=292$ K is in agreement with previous measurements of Lin *et al.*[16] and Mao *et al.*[14] and calculations of Ignatov *et al.*[24] [It should be noted that our specific heat data were corrected by carbon contribution (see Fig. 3), without this correction

TABLE III. Characteristic phonon frequency and coupling parameters derived by analyzing the experimental data of the present $MgC_{1.6}Ni_3$ sample.

		c_p analysis		H_{c2} analysis
		Normal state (Sec. V A)	sl state (Sec. V B)	(Sec. VI A)
ω_{ln}	[K]	143	88–134	
λ_{ph}		1.91	1.95–2.38	1.74–1.78[a]
λ_{sf}		0.43		

[a]Limited to band "1" $\doteq\lambda_{ph,h}$.

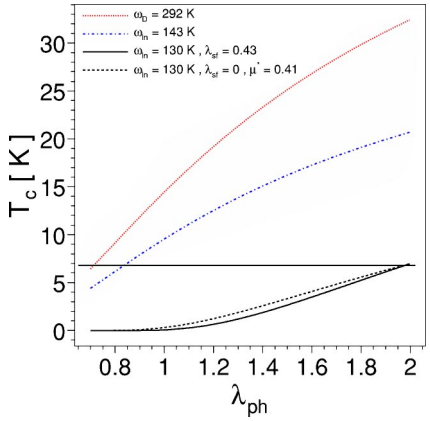

FIG. 24. (Color online) Variation of T_c with λ_{ph} without electron-paramagnon interaction and "normal" Coulomb pseudopotential $\mu^*=0.13$ according to Eq. (23) (dotted line) and Eq. (5) (dash-dotted line) and with enhanced pair-breaking contribution according to Eq. (8) by $\mu^*=0.13$ and $\lambda_{sf}=0.43$ (solid line), and $\mu^*=0.41$ and $\lambda_{sf}=0$ (dashed line), respectively. The characteristic phonon frequencies are chosen from Sec. IV B (dotted line), Sec. V A (dash-dotted line), and Sec. V B (solid and dashed line), respectively. The points of intersection of the curves with the horizontal line at $T_c=6.8$ K show the electron-phonon coupling strengths λ_{ph} resulting in the different approaches.

we arrive at $\Theta_D^*=285$ K]. In this analysis the McMillan formula

$$T_c=\frac{\omega_D}{1.45}\exp\left[-1.04\frac{1+\lambda_{ph}}{\lambda_{ph}-\mu^*(1+0.62\lambda_{ph})}\right] \qquad (23)$$

is usually applied. This approximation is only useful for a special phonon spectrum with $\omega_{ln}/\omega_D\approx 0.6$. In the case of $MgCNi_3$ we found $\approx 0.30-0.49$ (corresponding to $\omega_{ln}\approx 88-143$ K) and the Allen-Dynes formula [Eq. (5)] should be applied instead.

Figure 24 compares both equations using $\Theta_D^*\equiv\omega_D=292$ K (dotted line) and $\omega_{ln}=143$ K (dash-dotted line), respectively. In both cases the Coulomb pseudopotential was fixed to $\mu^*=0.13$. Apart from the deviation between Eqs. (5) and (23) due to the ratio $\omega_{ln}/\omega_D\leqslant 0.49$, both equations seem to result in a moderate electron-phonon coupling of $\lambda_{ph}=0.67-0.82$ if no additional pair breaking effects are considered.

However, we remind the reader that the experimental and theoretical picture of $MgCNi_3$ strongly indicates strong electron-phonon coupling and a spin fluctuation contribution. The solid line compared to the dash-dotted line in Fig. 24 shows that the dependence of T_c on λ_{ph} is strongly influenced by pair-breaking contributions such as the presence of enhanced electron-paramagnon coupling $\lambda_{sf}=0.43$. The same situation in the imaginable case of purely static pair breaking, expressed by $\mu^*=0.41$ is given by the dotted line. A very similar result was reported by Ignatov *et al.*[24] who proposed a phonon-softening scenario with $T_c=8$ K, $\omega_{ln}=120$ K, $\lambda_{ph}=1.51$, and an enhanced $\mu^*=0.33$ due to spin fluctuations. In any case the superconducting transition temperature is strongly suppressed by pair-breaking contributions.

T_c of $MgCNi_3$ would rise up to ≈ 20 K, if one somehow could suppress the electron-paramagnon interaction. In that case the electron-phonon coupling would not be affected and the dash-dotted line in Fig. 24 would become reality.

Within the phonon-softening scenario,[24] which was recently observed in neutron-scattering measurements,[39] a part of the low-temperature specific heat anomaly may be of phonon origin (as stated in Sec. V A). In this picture the electron-paramagnon coupling would be reduced with the possibility of a paramagnon shift to higher temperatures. This is consistent with $\omega_{ln}\approx 100$ K (lower limit of the result from Sec. V B) and an electron-paramagnon coupling constant of $\lambda_{sf}\approx 0.25$. Using these numbers in Eq. (8) the electron-phonon coupling constant amounts to $\lambda_{ph}\approx 1.7$. To find the composition of the phonon and paramagnon contribution to the upturn, low-temperature neutron-scattering measurements should be performed. In this context we remind the reader that spin fluctuations are known to show a dependence on the applied magnetic field, which indeed is seen in Fig. 12.

It was already mentioned that Hall data[8,15] and thermopower measurements[10] suggest electronlike charge carriers, whereas band structure calculations suggest holelike charge carriers. This puzzle can be resolved within an ITB model. The different gap values indicated from tunneling measurements[14,19] (large gap) and NMR measurements[7] (small gap) are also naturally explained by an ITB model, since in that case tunneling measurements measuring a current are most sensitive to large Fermi velocities just present in the electron band.

In view of this unclear situation, the multiband influence should not be fully neglected, since measured quantities would be affected oppositional by strong coupling and multiband effects. The aim of this section is to briefly analyze how multiband effects influence the specific heat, if at all.

Starting from the band structure calculations presented in Sec. II, the effect of interband scattering in $MgCNi_3$ is expected to be weak due to the presence of well-disjoint FSS's (like in the case of MgB_2). However, in contrast to MgB_2, one band dominates the density of states, resulting in a less-pronounced two-band character of $MgCNi_3$.

The total electron-phonon coupling constant averaged over all Fermi surface sheets, λ_{ph}, was estimated by Eq. (9) as $\lambda_{ph}=1.84$. Considering the band structure calculation, this value is distributed among the two effective band complexes according to

$$\lambda_{ph}=\lambda_{ph,h}\frac{N_h(0)}{N(0)}+\lambda_{ph,el}\frac{N_{el}(0)}{N(0)}. \qquad (24)$$

With $\lambda_{ph,h}=1.74-1.78$ (see Sec. VI A), the coupling in the second band amounts to $\lambda_{ph,el}=2.20-2.42$ [using $N_h(0)=0.85N(0)$ and $N_{el}(0)=0.15N(0)$]. Obviously this strong mass enhancement in both bands is not compatible with the low value of $T_c=6.8$ K. So as in the single-band case a considerable pair-breaking contribution in both bands is needed. In view of two different gaps, as suggested by comparing results from NMR[7] and tunneling[14,19] experiments, we introduce the gap ratio $z=\Delta_h/\Delta_{el}$. Within the BCS model used to

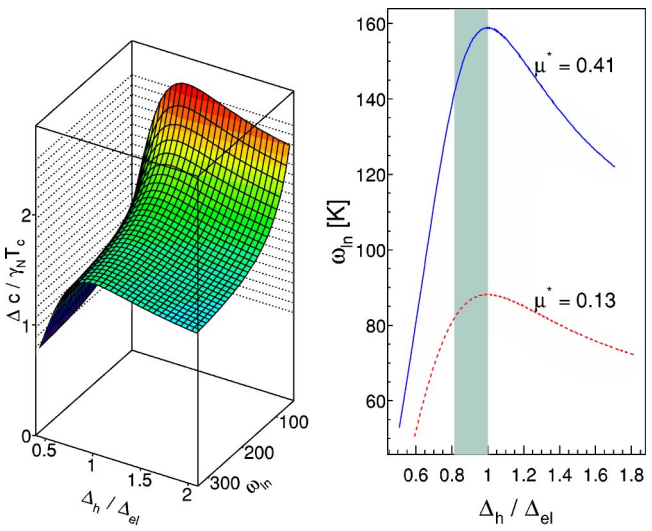

FIG. 25. (Color online) Left panel: dependence of the specific heat jump $\Delta c/\gamma_N T_c$ on the gap ratio Δ_h/Δ_{el} and the characteristic phonon frequency ω_{ln} within the two-band description for $\mu^*=0.13$. Right panel: possible solutions for Δ_h/Δ_{el} and ω_{ln} to reach the experimental specific heat jump for the two cases $\mu^*=0.13$ and $\mu^*=0.41$ (enhanced pair breaking). The gray area marks the range of expected Δ_h/Δ_{el} values (see Sec. V B).

describe the electronic specific heat in the superconducting state (Fig. 15), no deviation from the exponential behavior in the temperature range of $2<T_c/T<6$ was found for $0.8<z<1.0$ [agreeing with $\lambda_{ph,el}>\lambda_{ph,h}$, derived from Eq. (24)].

The dependence of the characteristic phonon frequency ω_{ln} on the parameter z and the pair breaking, expressed by an enhanced Coulomb pseudopotential, is shown in Fig. 25. The right panel indicates that the main difference between $\omega_{ln}=143$ K (derived from the normal-state analysis) and $\omega_{ln}=88$ K (derived from the specific heat jump analysis) is due to enhanced depairing, not considered by Eq. (12). The error in ω_{ln} due to multiband effects can thus be estimated as $\approx 10\%$ for $z=0.8$.

VII. CONCLUSIONS

Our analysis of $MgCNi_3$ revealed a highly interesting interplay of different, at first glance unexpected adversed physical features or tendencies all present within one material causing a rather complex general behavior. This novel superconductor has been interpreted so far as standard *s*-wave BCS superconductor or as unconventional superconductor with strong or medium electron-phonon coupling. Last but not least, a considerable pair-breaking contribution due to spin fluctuations and/or Coulomb repulsion have been suggested from theory and experiment.

The present analysis is the first approach to reconcile the unusual experimental findings within a unified physical picture. It reveals strong electron-phonon coupling combined with medium electron-paramagnon coupling. Strong electron-phonon coupling was derived from specific heat data in the normal and superconducting states independently. An unusual upturn of the specific heat in the normal state observed at low temperatures can be attributed to spin fluctuations and/or a softening of low-frequency phonons. To specify the contribution of the electron-boson interactions to the low-temperature specific heat anomaly, low-temperature neutron measurements are necessary in order to investigate the evolution of the lattice excitations, which may even be modified by the transition from the normal to the superconducting state.

The electronic specific heat data show an exponential temperature dependence at low temperatures which is a strong indication for *s*-wave superconductivity in $MgCNi_3$. It was shown that a contribution of a second band could not be excluded but even complies with recent tunneling measurement results. The multiband character of $MgCNi_3$ is proved by band structure calculations. However, with respect to the specific heat, the two-band character of $MgCNi_3$ is much less pronounced than, for instance, compared with the ITB model compound MgB_2. That is due to the predominance of a hole band with a large density of states in $MgCNi_3$, whereas in MgB_2 the densities of states of both bands are comparable. Therefore, several properties such as the specific heat or the upper critical field can be described to first approximation reasonably well within an effective single-band model. Nevertheless, other properties such as the Hall conductivity and the thermopower clearly require a multiband description—i.e., taking into account at least one effective electron and one effective hole band. Previous theoretical analyses based on single-band models could describe only few physical properties. As a consequence of the oversimplified approaches they blamed the local density approximation to fail seriously. This is in sharp contrast to our analysis of the upper critical field yielding an effective Fermi velocity agreeing well with the LDA hole band prediction. Our proposed effective two-band strong coupling approach explains the complex behavior observed for $MgCNi_3$ and is expected to hold for other still not examined physical properties.

The highly interesting interplay of strong electron-phonon coupling on multiple Fermi surface sheets, softening of lattice excitations, the strong energy dependence of the density of states near the Fermi energy of one band (Van Hove singularity), and paramagnons or strong Coulomb repulsion for a realistic, anisotropic multiband electronic structure with nesting features in this compound highly motivates further experimental studies. Investigating the influence of impurities or slight stoichiometry deviations on the electronic and bosonic properties would be as helpful as making of purer samples and single crystals to perform quantum oscillation studies like de Haas–van Alphen measurements.

Deepened theoretical studies are needed to clarify remaining quantitative details and to extend the present-day strong coupling Eliashberg theory with all peculiarities of $MgCNi_3$.

ACKNOWLEDGMENTS

The DFG (Grant No. SFB 463), the Emmy Noether Program (H.R.), and the NSF (Grant No. DMR-0114818) are gratefully acknowledged for financial support. We thank A. Ignatov, S. Savrasov, I. Mazin, W. Pickett, and T. Mishonov for discussions.

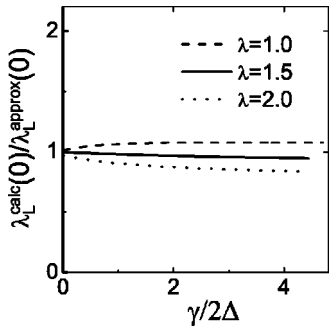

FIG. 26. Results of strong coupling calculations for the penetration depth at zero temperature [Eq. (A1)] for several electron-phonon coupling constants λ vs impurity scattering rate γ_{imp} (in units of the gap $\Delta_{exp}=1.1$ meV as derived from Sec. V B) in comparison with the approximate expression provided by Eq. (18).

APPENDIX: PENETRATION DEPTH—STRONG COUPLING AND IMPURITY SCATTERING

We present a simple semianalytic expression for the penetration depth at $T=0$ K for type-II superconductors valid in the London limit. Thereby strong coupling and impurity scattering effects are treated on equal footing within standard Eliashberg theory. In calculating $\lambda_L(0)$ we start from an expression proposed first by Nam[61] and later on frequently used in the literature:[62–64]

$$\lambda_L^{-2}(0) = \frac{\pi T \omega_{pl}^2}{c^2} \sum_{n=1}^{\infty} \frac{\Delta^2(i\omega_n)}{Z(i\omega)[\omega_n^2 + \Delta^2(i\omega_n)]^{3/2}}, \qquad \text{(A1)}$$

where $i\omega_n = i\pi(2n-1)T$, $n=0,\pm1,\pm2,\ldots$, are the Matsubara frequencies and $Z(i\omega_n)$ as well as $\Delta(i\omega_n)$ denote the renormalization factor and the gaps, respectively. The result of our numerical calculations of Eq. (A1) compared with the approximation given by Eq. (18) is shown in Fig. 26.

One realizes only small deviations not exceeding 8%–10% which is sufficient for our qualitative estimate of large mean free paths l_{imp} compared with the coherence length $\xi_{GL}(0)$.

*Electronic address: fuchs@ifw-dresden.de
†On leave from Int. Lab. of High Magn. Fields, Wroclaw, ISSP-BAS, Sofia, Bulgaria.
‡On leave from Inst. for High Pressure Physics, Troitsk, 142190, Russia.
§On leave from Inst. of Spectroscopy, Troitsk, 142190, Russia.

[1] T. He *et al.*, Nature (London) **411**, 54 (2001).
[2] H. Rosner, R. Weht, M. D. Johannes, W. E. Pickett, and E. Tosatti, Phys. Rev. Lett. **88**, 027001 (2002).
[3] S. B. Dugdale and T. Jarlborg, Phys. Rev. B **64**, 100508(R) (2001).
[4] D. J. Singh and I. I. Mazin, Phys. Rev. B **64**, 140507(R) (2001).
[5] A. Szajek, J. Phys.: Condens. Matter **13**(26), L595 (2001).
[6] J. H. Shim, S. K. Kwon, and B. I. Min, Phys. Rev. B **64**, 180510(R) (2001).
[7] P. M. Singer, T. Imai, T. He, M. A. Hayward, and R. J. Cava, Phys. Rev. Lett. **87**, 257601 (2001).
[8] S. Y. Li *et al.*, Phys. Rev. B **64**, 132505 (2001).
[9] T. G. Kumary, J. Janaki, A. Mani, S. M. Jaya, V. S. Sastry, Y. Hariharan, T. S. Radhakrishnan, and M. C. Valsakumar, Phys. Rev. B **66**, 064510 (2002).
[10] S. Y. Li *et al.*, Phys. Rev. B **65**, 064534 (2002).
[11] M. A. Hayward, M. K. Haas, A. P. Ramirez, T. He, K. A. Regan, N. Rogado, K. Inumaru, and R. J. Cava, Solid State Commun. **119**, 491 (2001).
[12] Q. Huang, T. He, K. A. Regan, N. Rogado, M. Hayward, M. K. Haas, K. Inumaru, and R. J. Cava, Physica C **363**, 215 (2001).
[13] S. Y. Li *et al.*, cond-mat/0104554v1 (unpublished).
[14] Z. Q. Mao, M. M. Rosario, K. D. Nelson, K. Wu, I. G. Deac, P. Schiffer, Y. Liu, T. He, K. A. Regan, and R. J. Cava, Phys. Rev. B **67**, 094502 (2003).
[15] D. P. Young, M. Moldovan, D. D. Craig, P. W. Adams, and J. Y. Chan, Phys. Rev. B **68**, 020501 (2003).
[16] J.-Y. Lin, P. L. Ho, H. L. Huang, P. H. Lin, Y.-L. Zhang, R.-C. Yu, C.-Q. Jin, and H. D. Yang, Phys. Rev. B **67**, 052501 (2003).
[17] S. V. Shulga, S.-L. Drechsler, G. Fuchs, K.-H. Müller, K. Winzer, M. Heinecke, and K. Krug, Phys. Rev. Lett. **80**, 1730 (1998).
[18] L. Shan, K. Xia, Z. Y. Liu, H. H. Wen, Z. A. Ren, G. C. Che, and Z. X. Zhao, Phys. Rev. B **68**, 024523 (2003).
[19] L. Shan, H. J. Tao, H. Gao, Z. Z. Li, Z. A. Ren, G. C. Che, and H. H. Wen, Phys. Rev. B **68**, 144510 (2003).
[20] R. Prozorov, A. Snezhko, T. He, and R. J. Cava, Phys. Rev. B **68**, 180502(R) (2003).
[21] D. P. Young, M. Moldovan, and P. W. Adams, Phys. Rev. B **70**, 064508 (2004).
[22] J. P. Carbotte, Rev. Mod. Phys. **62**, 1027 (1990).
[23] I. R. Shein, A. L. Ivanovskii, E. Z. Kurmaev, A. Moewes, S. Chiuzbian, L. D. Finkelstein, M. Neumann, Z. A. Ren, and G. C. Che, Phys. Rev. B **66**, 024520 (2002).
[24] A. Y. Ignatov, S. Y. Savrasov, and T. A. Tyson, Phys. Rev. B **68**, 220504(R) (2003).
[25] K. Koepernik and H. Eschrig, Phys. Rev. B **59**, 1743 (1999).
[26] Rietveld refinement program FULLPROF 2000.
[27] Z. A. Ren, G. C. Che, S. L. Jia, H. Chen, Y. M. Ni, G. D. Liu, and Z. X. Zhao, Physica C **371**, 1 (2002).
[28] A. F. Ioffe and A. R. Regel, Prog. Semicond. **4**, 237 (1960).
[29] N. F. Mott, Philos. Mag. **26**, 1015 (1972).
[30] P. H. Keesom and N. Pearlman, Phys. Rev. **99**, 1119 (1955).
[31] G. Fuchs, K.-H. Müller, A. Handstein, K. Nenkov, V. N. Narozhnyi, D. Eckert, M. Wolf, and L. Schultz, Solid State Commun. **118**, 497 (2001).
[32] N. R. Werthammer, E. Helfand, and P. C. Hohenberg, Phys. Rev. **147**, 295 (1966).
[33] C. Kittel, *Introduction to Solid State Physics*, 7th ed. (Wiley, New York, 1996).
[34] G. P. Srivastava, *The Physics of Phonons* (Adam Hilger, London, 1990).
[35] ROOT, an object-oriented data analysis framework v3.03, CERN,

Geneva, 2002.
[36] A. Junod, T. Jarlborg, and J. Muller, Phys. Rev. B **27**, 1568 (1983).
[37] S. Manalo, H. Michor, M. El-Hagary, G. Hilscher, and E. Schachinger, Phys. Rev. B **63**, 104508 (2001).
[38] P. B. Allen and R. C. Dynes, Phys. Rev. B **12**, 905 (1975).
[39] R. Heid, B. Renker, H. Schober, P. Adelmann, D. Ernst, and K.-P. Bohnen, Phys. Rev. B **69**, 092511 (2004).
[40] D. Rainer, Prog. Low Temp. Phys. **10**, 371 (1986).
[41] Strictly speaking, the Coulomb pseudopotential renormalized by the interaction with both bosons should read as $\mu^*[1+0.6(\lambda_{ph}-\lambda_{sf})]$. However, the accuracy of the calculated relative change of T_c is affected by the accuracy of the T_c expression used for the case without paramagnons. As a result, depending on the concrete parameter sets, either Eq. (8) or the corresponding expression with the renormalization of μ^* mentioned above yields a slightly better description of our numerical data. Anyhow, for the case of a strong el-ph interaction considered here, the difference between both appoximate expressions can be ignored. The interested reader is referred to a forthcoming paper by S. V. Shulga *et al.*
[42] S. K. Bose, O. V. Dolgov, J. Kortus, O. Jepsen, and O. K. Andersen, Phys. Rev. B **67**, 214518 (2003).
[43] G. Gladstone, M. A. Jensen, and J. R. Schrieffer, *Superconductivity* (Dekker, New York, 1969).
[44] H. Michor, R. Krendelsberger, G. Hilscher, E. Bauer, C. Dusek, R. Hauser, L. Naber, D. Werner, P. Rogl, and H. W. Zandbergen, Phys. Rev. B **54**, 9408 (1996).
[45] B. Mühlschlegel, Z. Phys. **155**, 313 (1959).
[46] J. E. Sonier, M. F. Hundley, J. D. Thompson, and J. W. Brill, Phys. Rev. Lett. **82**, 4914 (1998).
[47] D. A. Wright, J. P. Emerson, B. F. Woodfield, J. E. Gordon, R. A. Fisher, and N. E. Phillips, Phys. Rev. Lett. **82**, 1550 (1999).
[48] A. P. Ramirez, N. Stücheli, and E. Bucher, Phys. Rev. Lett. **74**, 1218 (1995).
[49] M. Hedo, J. Phys. Soc. Jpn. **67**, 272 (1998).
[50] M. Nohara, M. I. F. Sakai, and H. Takagi, J. Phys. Soc. Jpn. **68**, 1078 (1999).
[51] M. Nohara, M. Isshiki, H. Takagi, and R. J. Cava, J. Phys. Soc. Jpn. **66**, 1888 (1997).
[52] D. Lipp, M. Schneider, A. Gladun, S.-L. Drechsler, J. Freudenberger, G. Fuchs, K. Nenkov, K.-H. Müller, T. Cichorek, and P. Gegenwart, Europhys. Lett. **58**, 435 (1998).
[53] K. Izawa, A. Shibata, Y. Matsuda, Y. Kato, H. Takeya, K. Hirata, C. J. van der Beek, and M. Konczykowski, Phys. Rev. Lett. **86**, 1327 (2001).
[54] E. Boaknin, R. W. Hill, C. Proust, C. Lupien, L. Taillefer, and P. C. Canfield, Phys. Rev. Lett. **87**, 237001 (2001).
[55] J.-Y. Lin and H. D. Yang, *Superconductivity Research at the Leading Edge*, edited by P. S. Lewis (Nova Science Publishers, Inc., New York, 2004).
[56] C. Q. Jin, Y. L. Zhang, Z. X. Liu, F. Y. Li, W. Yu, and R. C. Yu, Physica C **388-389**, 561 (2003).
[57] V. A. Moskalenko and M. E. Palistrant, *Statistical Physics and Quantum Field Theory* (Nauka, Moscow, 1973).
[58] A. Wälte, G. Fuchs, K.-H. Müller, A. Handstein, K. Nenkov, V. N. Narozhnyi, S.-L. Drechsler, S. V. Shulga, L. Schultz, and H. Rosner, cond-mat/0402421 (unpublished).
[59] S. V. Shulga and S.-L. Drechsler, J. Low Temp. Phys. **129**(1-2), 93 (2002).
[60] A. Karkin, B. Goshchitskii, E. Kurmaev, Z. A. Ren, and G. C. Che, cond-mat/0209575 (unpublished).
[61] S. B. Nam, Phys. Rev. **156**, 470 (1967).
[62] F. Marsiglio, J. P. Carbotte, and J. Blezius, Phys. Rev. B **41**, 6457 (1990).
[63] S. D. Adrian, M. E. Reeves, S. A. Wolf, and V. Z. Kresin, Phys. Rev. B **51**, 6800 (1995).
[64] A. A. Golubov, A. Brinkman, O. V. Dolgov, J. Kortus, and O. Jepsen, Phys. Rev. B **66**, 054524 (2002).